A Fundamental Study of DC/RF Breakdown and Corona of Atmospheric Air

by

Ivan Alexander Aponte, B.S.E.E.

A Thesis

In

Electrical Engineering

Submitted to the Graduate Faculty
of Texas Tech University in
Partial Fulfillment of
the Requirements for
the Degree of

MASTER OF SCIENCE IN ELECTRICAL ENGINEERING

Approved

Dr. Andreas Neuber
Chair of Committee

Dr. Jacob Stephens

Dr. Mark Sheridan
Dean of the Graduate School

December, 2020

ACKNOWLEDGEMENTS

TABLE OF CONTENTS

ABSTRACT

Radio frequency (RF) breakdown in air at a frequency relevant to ionospheric heating – 3.3 MHz, is studied at centimeter-sized gap distances and is compared to literature and simulations. To establish a point of reference, DC breakdown using spherical and Bruce profile electrodes was measured and subsequently extended to examine RF breakdown. Various electrode combinations were tested to which brass cathodes created the largest variance in the datasets for DC tests. Gap distances from 1-10 mm were tested for both DC and RF breakdown with the slow-rise envelope (5 mV/μs) RF breakdown occurring at approximately 80% of the DC breakdown value, a value supported by Monte Carlo simulations. Increasing the envelope rise-time of the RF voltage yielded RF breakdown voltage that was roughly 20% higher than the DC breakdown value in addition to increased amplitude fluctuations. Illuminating the electrode gap with UV minimized the breakdown amplitude fluctuations due to photoemission at the electrodes. Through UV ICCD imaging of pre-breakdown, it was found that RF breakdown tends to favor a single channel. It is postulated that once ionization begins, the current favors the spot where the first ionization occurred creating a stronger channel in that location and the ultimate breakdown event.

Finally, to address real world geometries with sharp corners or protrusions, DC and RF corona behavior utilizing tungsten needles of varying tip angle geometry and materials – 2 % Lanthanated and pure – in a needle-plane configuration is investigated. A photomultiplier tube (PMT) was used to detect corona before visible light emission for a more accurate understanding of when corona onset occurs. The obtained results help us define the operation limits of high-power antennas at 1-10 MHz frequencies.

LIST OF TABLES

LIST OF FIGURES

CHAPTER 1

INTRODUCTION

The motivation behind this study of RF breakdown and corona at 3.3 MHz in atmospheric air is to quantify the power limitations of a tunable electrically small antenna (ESA) design [6, 19, 20], see Fig. 1.1. The ESA has a frequency range of 3-10 MHz and is tuned by changing the capacitance of its parallel plate gap. At 3 MHz and 500 kW power levels, the capacitive gap yields the highest electric fields exceeding 20 kV/cm and is most susceptible to forming corona or initiating breakdown. To recreate the conditions of the ESA in the experimental setup, an RF signal is fed into a highly resonant loosely coupled LC tank circuit that generates high RF voltages at the electrode gap.
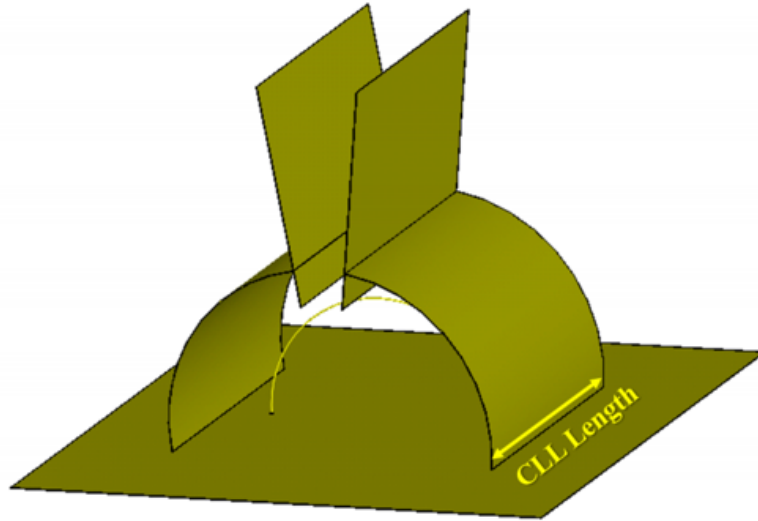
Figure 1.1. 3D model of tunable ESA for ionospheric heating research [6].

Breakdown under alternating fields has been studied ranging from power frequencies [21] up to microwave frequencies (1 GHz and above) [22]. One of the earliest accounts of RF breakdown being studied is Reukema's work utilizing spherical electrodes in atmospheric air at frequencies from 60 Hz to 425.5 kHz [23]. Reukema observes a gradual decrease in breakdown voltage between 20-60 kHz and attributes

this behavior to ion mobility [1]. Other works studying RF breakdown at this frequency range have come to this conclusion as well [24, 25]. At single digit MHz frequencies in centimeter sized air gaps, this behavior is most pronounced, yielding breakdown fields at approximately 80% of the DC breakdown value.

RF corona has been studied by several researchers for various works. Sato and Haydon observed the onset and formation of 10 MHz corona in a needle-plane geometry over 80-650 torr [26]. Sakiyama and Graves study and provide evidence of two different discharge modes of RF corona at atmospheric pressure [27]. Their work is centered on 13.56 MHz corona in a needle-plane geometry, which is referred to as the 'plasma needle' and is relevant to biomedical applications. Other workers have investigated the optical emission spectrum [28] and the physical discharge characteristics with respect to voltage-power curves [29] for the plasma needle. Auzas measured the electrical and thermal properties of 5 MHz pulsed RF corona at pressures greater than 1 bar [30] and developed a model for it [31]. Price et. al derived a breakdown criterion for low and high frequency corona of an isolated cylindrical monopole using the electron continuity equation [32].

From performing a literature survey, it is noted that the body of work performed for RF breakdown and corona is not nearly as expansive as its DC counterpart. In addition to quantifying the threshold power to mitigate breakdown in the ESA, the goal of the work presented in this thesis is to extend the available literature for RF breakdown and corona at single digit MHz frequencies in atmospheric conditions. Different components of RF breakdown and corona were measured and analyzed to fill in the gaps in the literature.

CHAPTER 2

THEORETICAL BACKGROUND

Before delving into the experimental setup and results, some background theory pertinent to the discussion of breakdown and corona must be covered first. The experimental study covers gaseous breakdown and corona under static and alternating fields, which requires an understanding of the underlying physical processes that govern them. In this chapter, the mechanisms of breakdown and corona under static and alternating fields will be covered briefly. For a more in depth discussion of these topics, one may refer to the referenced literature [1,11,12]. Additionally, a few topics relevant to the experimental setup will be discussed as well.

2.1 Ionization

There are a number of mechanisms that generate electrons needed to initiate breakdown and corona process. The mechanism in which an atom or molecule that absorbs enough energy to free one of its electrons and becomes positively charged is referred to as ionization. The product of ionization is a positive ion and the emitted electron. The same positive ion can be ionized multiple times and assume a charge (+ne) where n is the number of ionizations and e is the electron charge. When an electron attaches itself to a neutral molecule, it assumes an overall negative charge and is referred to as a negative ion. A positive ion will return to its neutral state when it recombines with a free electron. The accumulation of ions largely contributes to the conductivity of a gas. Therefore, it is paramount to understand ionization and its role in gas discharge processes. While several mechanisms exist that can ionize or excite atoms or molecules, only ionization via electron collisions and photons (photoionization) will be covered here. Ionization/excitation by collisions are the dominant mechanism in the breakdown and corona process. It is noted that photoionization is a necessary process involved in the formation of anode (positive) corona.

3

2.1.1   Ionization By Collisions

The generation of secondary electrons by collisions plays a very significant role in creating space charges in a gas. In an electrode gap fed with a bias voltage, a free electron will gain kinetic energy as it accelerates in the electric field and make collisions with a neutral molecule. If the kinetic energy that the electron imparts onto the neutral gas molecule is large enough, the gas molecule will become excited or ionized. Collisions that result in ionization event caused by the exchange of kinetic are called collisions of the first order [1].

$$A + e \rightarrow A^+ + 2e \quad (Direct\ ionization)$$

$$A + e \rightarrow A^* + e \quad (Excitation\ by\ electron\ to\ atom\ collision)$$
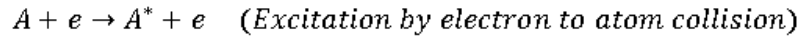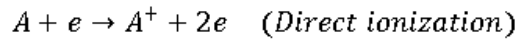
Collisions of the second order are collisions in which ionization is caused by the exchange of potential energy [1]. This type of collision involves an already excited atom, which was excited by a collision of the first order or a different process. An example of a collision of the second order is the Penning effect, which consists of ionization by an excited atom colliding into a neutral atom. It is noted that the second order collisions described below make little impact on the secondary electron generation needed in the breakdown process. Rather, collisions causing direct ionization are the main contributor to growing the electron population in the gap needed to initiate breakdown.

$$e + A^* \rightarrow A + e \quad (Higher\ energy\ electron)$$

$$A^* + B^* \rightarrow A + B^+ + e \quad (Ionization\ by\ collision\ of\ two\ excited\ atoms)$$

$$A^* + B \rightarrow A + B^+ + e \quad (Penning\ effect)$$
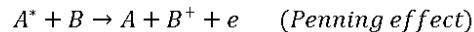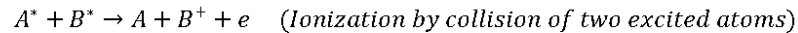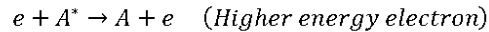
Those studying gas discharge are typically interested in knowing the value of the number ionizations an electron makes when colliding with neutral atoms/molecules while moving from cathode to anode. This value, known as Townsend's first ionization coefficient, is denoted as α and is given by the number ionizations per unit length. Townsend's first ionization coefficient, α, can be written as

4

$$\alpha = Ape^{-Bp/E} \tag{2.1}$$

where p is the pressure of the gas and E is the electric field between the anode and cathode. A and B are gas constants that were found empirically through discharge experiments. The gas constants for various gasses, which are suitable for quick estimates (with limited range of validity), from literature [1] are tabulated below:

Table 2.1. The constants A and B for various gases [1]

Gas	A (ionizations/cm^{-1}torr^{-1})	B (V/cm^{-1}torr^{-1})	E/p Validity Range (V/cm^{-1}torr^{-1})
Air	15	365	100-800
N$_2$	12	342	100-600
H$_2$	5.1	138.8	20-600
He	3	34	20-150
Ne	4	100	100-400
A	14	180	100-600
Kr	17	240	100-1000
Xe	26	350	200-800

While knowing the number of secondary electrons created via ionization is a good start, it is still incomplete. Electron attachment, a loss mechanism that removes electrons in the ionization region, must be considered to arrive to a more accurate value of the number of ionizations per unit length. Electronegative gases such as O_2 are responsible for electron attachment in atmospheric air, so it is especially important to account for electron attachment when calculating the overall degree of ionization in an electrode gap. The effective ionization coefficient which factors in electron attachment is found by

$$\alpha_e = \alpha - \eta \tag{2.2}$$

where η is the electron attachment coefficient given in the number attachments per unit length. Tabulated values for measured α/p and η/p, the reduced ionization and attachment coefficients, at different levels of E/N are reported below [2]:

Table 2.2. Ionization and Attachment Coefficients in Dry Air at Low Values of E/N [2]

E/N	α/N	η/N	E/N	α/N	η/N
80		1.45(-3)			
95	0.0001	1.6(-3)	130	0.0086	
100	0.0002		135	0.0105	
105	0.0009		140	0.0126	2.1(-3)
110	0.0020	1.80(-3)	150	0.0174	
120	0.0047		160	0.0224	
125	0.0066	1.98(-3)	170	0.0278	

E/N in units of Td, coefficients in units of 10^{-20} m^2. a(b) means a x 10^b

It is noted that using Eq. 2.1 to calculate α for DC breakdown of atmospheric air in 1-10 mm gaps is not feasible due to the E/p being outside the validity range for the gas constants for air, c.f Table 2.1. As an alternative, equations for alpha for air taken from Sarma and Janischewskyj, which are a best fit of experimental measurements by Harrison and Geballe [33], Masch [34], and Sanders [35], can be used instead. The equation for η for air that Sarma and Janischewskyj also produced, which is a best fit of data taken by Harrison and Geballe [33], can also be used to calculate α_e. The equations α/p and η/p and their validity ranges expressed as E/p [V/$cm^{-1}torr^{-1}$] are repeated below [8].

$$\alpha/p = 4.7786e^{(-221p/E)}, 25 \leq E/p \leq 60 \ V/cm^{-1} \cdot torr^{-1} \tag{2.3}$$

$$\alpha/p = 9.682e^{(-264.2p/E)}, 60 \leq E/p \leq 240 \ V/cm^{-1} \cdot torr^{-1} \tag{2.4}$$

$$\eta/p = 0.01298 - 0.541 \cdot 10^{-3}E/p + 0.87 \cdot 10^{-5}(E/p)^2, 25 \leq E/p \leq 60 \ V/cm^{-1} \cdot torr^{-1} \tag{2.5}$$

Sarma and Janischewskyj notes that the contribution of attachment on α at higher values of E/p is negligible [8]. Thus, Eq. 2.4 is not corrected for attachment. α_e for atmospheric air was also calculated using MultiBolt, a multi-term Boltzmann equation model that calculates electron swarm parameters for low temperature plasma models [7]. MultiBolt is validated and uses well characterized cross-sections for its calculations. Thus, Multibolt is believed to produce the most reliable value for α_e. α_e using the equations produced by Sarma and Janischewskyj, Multibolt, and Eq. 2.1 are graphed below, see Fig. 2.1.
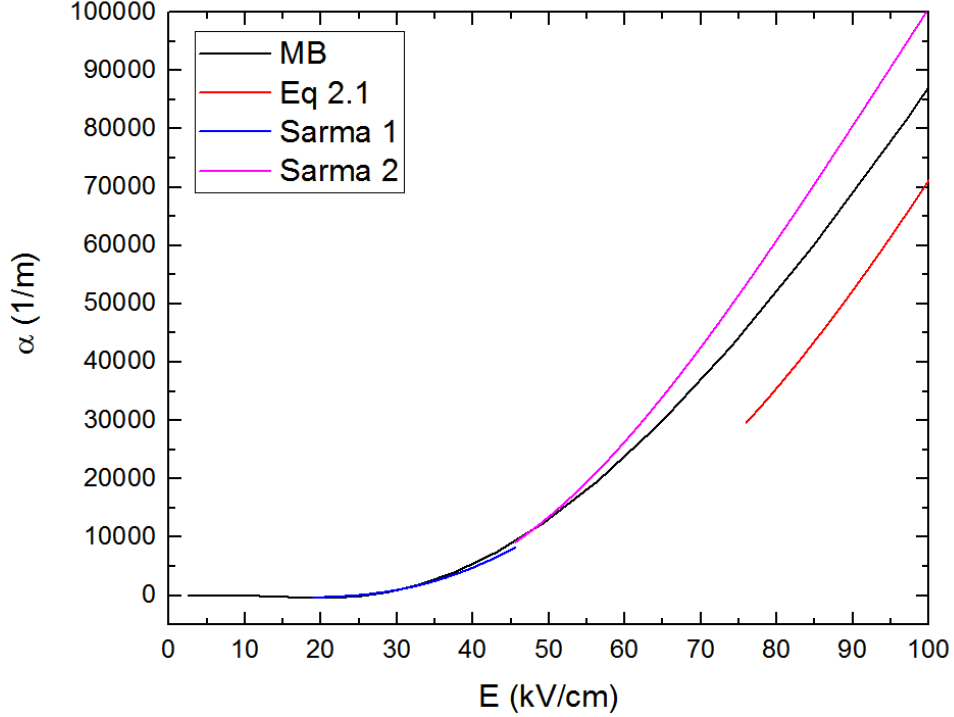
Figure 2.1. First Townsend coefficient α vs E for atmospheric air. MB: α_e calculated using MultiBolt [7]; Sarma 1 : α_e using Eq. 2.3 and 2.5 [8]; Sarma 2: α_e using Eq. 2.4 [8].

2.1.2 Photoionization

An electron with a lower energy than the ionization energy of the molecule it collides with will raise the atom to a higher energy state. After a short time ($10^{-10} - 10^{-7}$ s), the electron will transition back to a neutral state by releasing the excess energy in the form of photon with a energy hν, where h is Planck's constant and ν is the frequency of the photon. The emitted photon can then ionize a molecule if its energy is higher than the ionization energy of the molecule. This process is known as photoionization. Photoionization is a secondary ionization process that may contribute to the Townsend mechanism and is necessary for streamer development and some corona discharges [12]. Photons that induce photoionization usually have shorter wavelengths (in the UV spectrum). For example, O_2 and N_2, the most abundant gases in atmospheric air, have ionization energies of 12.07 and 15.58 eV, respectively. At a

minimum, the wavelength of the photon must be less than 102 nm, which is well into the vacuum UV range (VUV).

2.2 Types of Emission

The emission of electrons and photons are fundamental to the discussion of gas discharges. Cathode processes such as secondary electron emission by ion impact and photoemission are the main contributors for driving the feedback mechanism for breakdown described by Townsend. This feedback mechanism for breakdown will be discussed further in a later section. In this section, spontaneous emission, photoemission, field emission, secondary emission by ion impact, and secondary emission from metastables are discussed in some detail.

2.2.1 Spontaneous Emission

An excited atom, likely excited by a collision process, will return to its ground state after a short time. When the excited electron returns to it ground state, it will release the energy it had gained from excitation in the form of a photon with energy $h\nu$, where h is Planck's constant and ν is the frequency of the photon. This process is referred to as spontaneous emission. A simple diagram representing the process of spontaneous emission is illustrated, see Fig. 2.2.
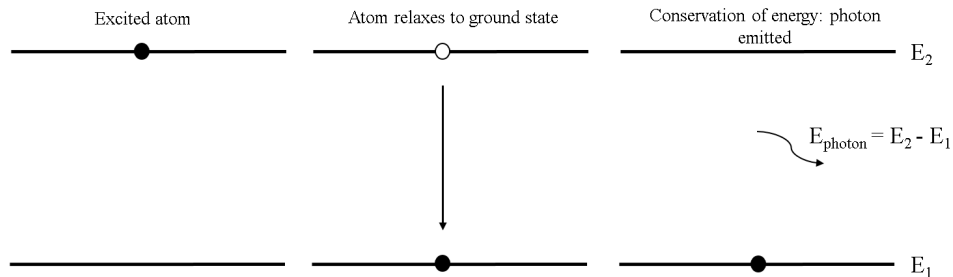
Figure 2.2. Spontaneous emission process.

The photon will be in emitted in a random direction and have a random phase. An excited atom does not necessarily have to make the drop to the its ground state in

one jump. It may drop to discrete energy levels that exist between the excited level and ground state before ultimately reaching the ground state. The emitted photon energy is found by

$$E_{photon} = E_2 - E_1 \tag{2.6}$$

where E_2 is the initial higher energy level and E_1 is the final lower energy level. The energy of the photon is expressed in electronvolts (eV), which refers to the amount of energy needed to move an electron under an electrostatic potential of 1 V. 1 eV is equal to $1.602 \cdot 10^{-19}$ J.

2.2.2 Photoemission

Photoemission, also called the photoelectric effect, is the emission of an electron from a metal surface when it is irradiated. Photoemission was first observed by Heinrich Hertz in his experiment with a spark gap generator [36] and was theorized by Einstein in 1905 [37]. When irradiated, an electron bound to the metal will absorb the photon energy. If the photon energy is larger than the work function of the metal, the energy needed to strip an electron from the surface of any given material, an photoelectron will be liberated from it. The maximum kinetic energy of the emitted photoelectron is written as

$$E_{kmax} = h\nu - \phi \tag{2.7}$$

where ϕ is the work function of the material that the photoelectron is emitted from. Tabulated values for the work function of metals are readily available in literature.

2.2.3 Field Emission

Field emission is the emission of electrons from a metal to a medium due to an electric field of high magnitude. A micro structure on the surface of a metal electrode will give rise to a locally enhanced electric field sufficient to cause field emission under a sufficiently high applied electric field. The field enhancement factor of the protrusion

β is found by dividing the maxixmum value of local field by the value of the applied electric field. Typically, field emission starts when the local electric field reaches magnitudes on the order of 10^9 to 10^{10} V/m. Fowler and Nordheim proposed the theory of field emission being due to electron tunneling; the probability of electrons in a solid to penetrate the potential barrier lowered by the applied electric field. Fowler and Nordheim considered this probability and produced an equation that expresses the number of electrons being emitted per unit time [38]. The Fowler-Nordheim equation in numerical form is written as

$$j_f = 6.2 \cdot 10^{-6} \frac{(\epsilon_F/\phi)^{1/2} E^2}{\epsilon_F + \phi} exp(\frac{-6.85 \cdot 10^7 \phi^{3/2} \zeta}{E}) \ [\frac{A}{m^2}] \tag{2.8}$$

where E is the field in V/cm, ϕ is the work function of the metal (typically around 4 eV), ϵ_F is the fermi energy in eV, and ζ is a correction factor for its reduction, see Table 4.9 in reference [11]. A more rigorous derivation of the Fowler-Nordheim equation can be found in [38].

2.2.4 Thermionic Field Emission

In the case where a strong electric field is applied to the surface of a heated metal, both the heat and electric field will have an impact on electron emission [11]. This is referred to as thermionic field emission or Schottky emission (SE). The current density for SE is given by

$$j_s = \frac{4\pi m_e e_c (kT)^2}{h^3} exp(\frac{e_c^{3/2} E^{1/2}}{(4\pi\epsilon_0)^{1/2} kT} - \frac{\phi}{kT}) \tag{2.9}$$

where m_e is the mass of an electron, e_c is the elementary charge, k is the Boltzmann constant, ϵ_0 is the vacuum permittivity, and T is the temperature of the metal [39]. It is noted that the SE equation is valid when the field is low enough to where the tunneling current is negligible. A measure of the tunneling current is given by the dimensionless equation

$$q = 1.656 \cdot 10^{-4} \frac{E^{3/4}}{T} \qquad (2.10)$$

where E is the electric field in V/m and T is the temperature in Kelvin [39]. For instance, a q of 0.5 translates to half of the current being due to tunneling. There is an extended form of the SE equation that is valid between $0 < q < 0.7$ [39]. The extended SE equation, j_{es}, takes the form of

$$j_{es} = j_s \frac{\pi q}{sin(\pi q)}. \qquad (2.11)$$

The transition between SE and the extended SE occurs at q=0.3. Beyond q=0.7, the extended SE equation becomes invalid.

2.2.5 Secondary Emission By Ion Impact

Secondary electrons may be emitted from metal surfaces by impact of positive ions or excited atoms. For this type of emission to occur, the impacting ion must liberate two electrons: one that neutralizes the ion and another that is emitted as the secondary electron. The minimum amount of energy required for an ion to emit two electrons is at least twice the work function of the metal surface that the ion is impacting. This condition can be expressed as

$$W_k + W_p \geq 2\phi_m \qquad (2.12)$$

where W_p and W_k are the respective potential and kinetic energies of the impacting ion and the ϕ_m is the work function of the metal [12]. Secondary emission by ion impact plays a minor role in the Townsend spark discharge mechanism. Photoemission is believed to be the principle process in the Townsend spark discharge mechanism (see section 2.3.1).

2.2.6   Secondary Emission By Metastables

Electrons may be liberated from a metal surface by atoms in the metastable state only if their energy is higher than the work function of the metal surface [1]. Metastable atoms have longer lifetimes than excited species. However, they cannot reach the cathode by being accelerated by the electric field since they do not carry charge. Rather, they reach the cathode via thermal diffusion. When considering a parallel plate gap that has a uniform electric field, a great number of metastables are lost due to diffusion to the anode or by diffusing out of the gap [1]. Only a fraction of the metastables reach the cathode to liberate secondary electrons. It is also important to note that this process is far slower than other processes such as photoemission or secondary emission by ion impact. The reason is that diffusion is slower than photons traveling at the speed of light or the positive ions traveling at a speed proportional to the electric field being applied. Metastables however may live longer than ions or electrons. Depending on the overall dynamics of the system, they may play a decisive role in repeated breakdown events (typically in the case of low pressure breakdown) [40].

2.3   Breakdown in Uniform Fields

This section will cover some of the fundamentals of DC and RF breakdown in uniform fields. Due to the motivation of the project being an ESA in atmospheric air, vacuum breakdown and breakdown at very large pressures will be neglected. The discussion begins with the second Townsend coefficient, γ. This is followed by the Townsend breakdown criterion, which takes γ into consideration. Then, the breakdown equation that is derived using the Townsend breakdown criterion, Paschen's law, is discussed. An empirical DC breakdown equation for air is also discussed since it is used to compare with the experimental DC breakdown measurements discussed in this thesis. The statistical and formative time delay of breakdown are covered as well. Finally, the mechanisms which separate RF breakdown from DC are discussed.

2.3.1   Second Townsend Ionization Coefficient

A parallel plate electrode configuration biased with a voltage forms a uniform electric field in the gap. An initiatory electron, for instance, originating from background radiation processes or cosmic rays, will enter the gap and accelerate towards the anode due to the electric field. As the electron moves along the gap, it will gain kinetic energy and eventually make a collision with neutral gas atom. The kinetic energy of the electron under the electric is found by

$$E = \frac{1}{2}mv_d^2. \tag{2.13}$$

The variable m is the mass of the electron and v_d is the average velocity of the electron under the influence of the electric field. The drift velocity is given by

$$v_d = -\mu E \tag{2.14}$$

where μ is the mobility which describes how quickly an electron can move in a medium in units of $\dfrac{cm^2}{V \cdot s}$.

If the initial electron had accumulated energy exceeding the ionization energy of the gas atom, the gas atom will become ionized and produce a secondary electron. The primary electron that had made the collision and the secondary electron will continue to accelerate in the electric field and make collisions again. These ionization processes become a chain reaction and lead to electron multiplication in the gap, otherwise known as an electron avalanche.

However, the electron avalanche will eventually reach the anode and become neutralized upon making impact. For breakdown to develop, there is required feedback mechanism which produces new electrons to be accelerated through the gap. This feedback mechanism for breakdown is known as Townsend's second ionization coefficient, γ. γ is composed primarily of several cathode processes lumped into one. One may find γ as

$$\gamma = \frac{\beta}{\alpha} + \gamma_i + \gamma_p + \gamma_m + ..., \tag{2.15}$$

where γ_i is secondary emission due to positive ion impact, γ_p is the secondary emission due to photons from excited gas, and γ_m is the secondary emission by metastables [1]. β/α is a ratio of the number of electrons an ion produces through collisions with gas molecules per unit length (β) to the number of ionization events that occur from cathode to anode per unit length (α). Nasser notes that the contribution of β is not significant in the total weight of γ due to the fact that positive ions cannot effectively ionize gas atoms at the fields in which breakdown occurs as it requires transit times longer that the actual time for breakdown event [1]. It is also noted that γ_i, which is responsible for photoemission of the cathode, is typically the dominant process rather than γ_i. It is also important to note that the value of γ varies with the electrode material, its surface conditions (such as surface roughness or contamination), and its cross section.

2.3.2   Townsend Breakdown Criterion

As the applied voltage between two electrodes in a gas increases, the current at the anode electrode will increase with accordance to

$$I = I_0 \frac{e^{\alpha d}}{1 - \gamma(e^{\alpha d-1})} \tag{2.16}$$

until a point is reached in which the dark current transitions to a self sustaining discharge [12]. If the external agent, I_0, is removed ($I_0{=}0$), then the current will die out. When the current transitions to a self sustaining discharge, the current then becomes indeterminate and takes the form

$$\gamma[exp(\alpha d) - 1] = 1 \tag{2.17}$$

which is the Townsend breakdown criterion. The number of ions produced by the first electron avalanche is sufficient enough that the resulting ions impacting the cathode are able to release a secondary electron to initiate a successor electron avalanche. A secondary electron may also be generated by photoemission at the cathode. At this point, there is a constant stream of electrons due to the initial electron avalanche and subsequent photoemission. When the left hand side of the Townsend breakdown criterion equation is greater than unity, the ionization produced by successive avalanches is cumulative. The spark discharge grows more rapidly the larger it exceeds unity.

2.3.3 Paschen's Law

Paschen's law decribes the breakdown voltage between two electrodes as a function of gas pressure and electrode gap distance, which was found empirically from the results of Friedrich Paschen's famous 2 sphere breakdown experiment in 1889. [41]. In the simple case where alpha can be expressed via Eq. 2.1, the breakdown equation takes the form of

$$V_b = \frac{Bpd}{ln\dfrac{Apd}{ln(1+1/\gamma)}}, \tag{2.18}$$

where p is the gas pressure and d is the electrode gap distance. A and B are the same gas constants mentioned in section 2.1.1. Typical values of γ for atmospheric air range from 0.001 to 0.01 [1]. Paschen's law is graphed for atmospheric air as function of gap distance below, cf. Fig 2.3.
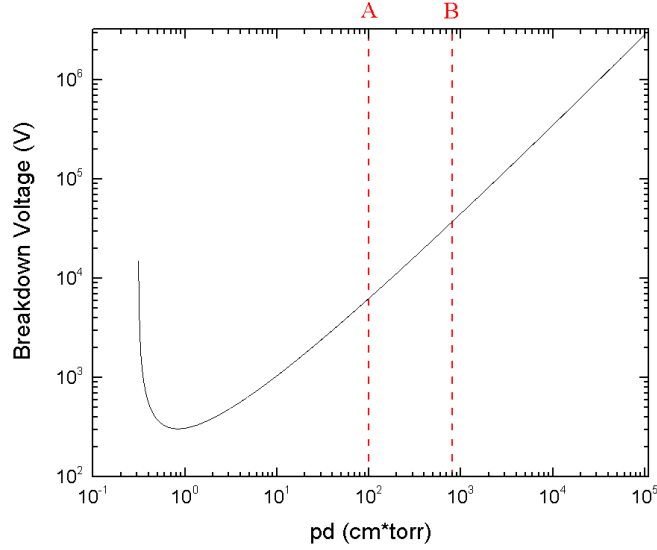
Figure 2.3. Equation 2.18 graphed for atmospheric air as a function of pd. $\gamma = 0.01$. Markers A and B show the validity range of Eq. 2.18 based on the tabulated gas constants for air given in Table 2.1.

When pd approaches 0, the equation fails. At low values of pd, V_b will reach a minimum value before rising up with increasing pd. This minimum value, known as the Paschen minimum, is defined as

$$V_{b(min)} = 2.718\frac{B}{A}ln(\frac{1}{\gamma} + 1). \tag{2.19}$$

The Paschen minimum is an important value to calculate for practical applications in which gaseous breakdown occurs. For atmospheric air, assuming γ values between 0.001 and 0.01, the Paschen minimum will float between 460 V to 300 V.

Some limitations of Paschen's law are noted and described in depth by Nasser [1]. At extremely large and low values of pd, there are deviations of V_b that have been observed that the law cannot capture. At low pressures, gas processes become less significant and breakdown will initiate from the electrode instead. At large pd, streamers are the main mechanism that govern breakdown rather than the Townsend mechanism. Streamers are covered in more detail in section 2.4.2. Paschen's law is also limited by the gas constants due to their validity in a specified range of E/p.

Similar to the situation with eq. 2.1, the breakdown voltage calculated by Paschen's law cannot be used to compare with the experimental DC breakdown measurements because E/p of the experimental measurements are outside of the validity range for the gas constants given for air. In the next subsection, an alternative breakdown for air is discussed.

2.3.4 DC Breakdown Equation for Air

After conducting an extensive literature survey, a suitable equation that describes DC breakdown for air was found. The breakdown equation described by Lau [9] (in kV), which is an empirical equation based on a fit of experimental values [17, 42, 43], is written as

$$V_s = 24.4pd + 6.53\sqrt{pd}, \tag{2.20}$$

where p is the gas pressure in torr and d is the gap distance in cm. The equation assumes a gas temperature at 20°C and is graphed below, cf. Fig 2.4. This equation works for gaps ranging from 0.1 mm to 20 cm. The Townsend breakdown mechanism is the dominant process at atmospheric pressure if the gap is not too large ($pd < 1000 \; cm \cdot torr$) and if the field is uniform [11]. Thus, uniform breakdown in atmospheric air with gaps ranging from 1-13 mmm are driven mainly by the Townsend mechanism.
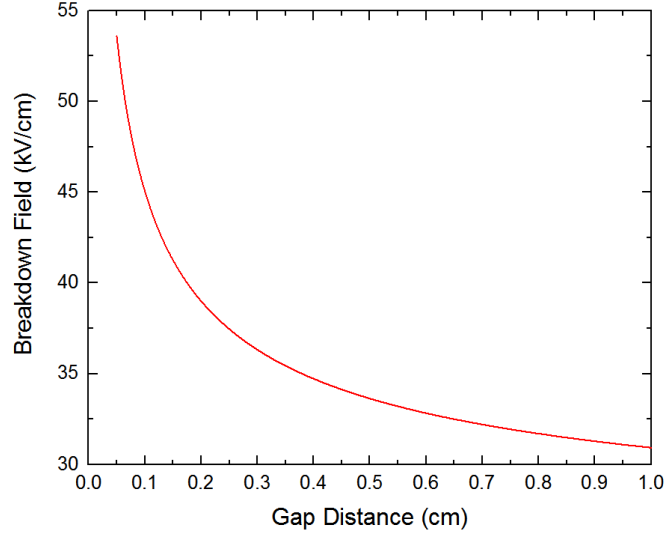
Figure 2.4. Lau breakdown equation for atmospheric air plotted for gaps ranging from 0.5 mm to 1 cm [9].

The comparison of the DC breakdown measurements with Lau's equation will be covered later in section 4.1.

2.3.5   Time Delay of Breakdown

One important aspect of breakdown is the time delay; the time that passes between application of sufficient voltage to initiate breakdown in a gap and the ensuing breakdown [12]. The time delay consists of two different components: the statistical time delay and the formative time delay. The statistical time delay is the time it takes for an initiatory electron to enter the gap to start the breakdown process and the formative time delay is the time it takes for the breakdown to develop once it is initiated. In cases where the applied voltage in gap is slowly increased over time, the statistical time delay is not applicable since there are usually initiatory electrons present originating from cosmic rays or natural background radiation sources [12]. However, statistical time delay must be considered when the applied breakdown voltage occurs over a short time scales (impulse voltage or voltage surge). One technique for reducing the statistical time delay is to irradiate the electrode surface with UV light. Doing this will seed electrons in the gap via photoemission from the electrode

19

surface. The statistical time delay may also be reduced by applying an overvoltage, a voltage much higher than the breakdown voltage, to the gap [12]. The formative time delay is largely dependent on the type of breakdown mechanism in question. Breakdown based on the Townsend mechanism involves the multiplication of electron avalanches via secondary cathode emission, which can yield formative time delays on the order of $10^{-6}s$ [1]. The formative time delay for breakdown via Townsend mechanism is quite long and could not explain breakdown on the fast time scales as observed in experiments (on the order of 10^{-8} s) [1]. A new breakdown mechanism based on streamers was born and adequately explained breakdown at fast time scales. Streamers develop on very short time scales and will yield a sudden increase of ionization intensity in the channel, creating the conditions for breakdown to occur [1]. In the case of breakdown of atmospheric air in uniform fields, gaps greater than 6 cm breakdown via the streamer mechanism and gaps less than 5 cm breakdown via avalanche multiplication [11]. The experimental DC breakdown data reported in the results section 4.1 are for 0.1 - 1 cm gaps, so the streamer mechanism does not apply. The initiation and development of streamers are covered in more detail in section 2.4.2.

2.3.6   RF Breakdown

The physical processes for breakdown change significantly under an alternating field. The electron and ion mobility under the RF field are the dominant mechanisms affecting the breakdown voltage. In low frequencies, the alternating field is not fast enough to impact the movement of the electrons or ions during one half cycle. At a certain critical frequency, the ions, which are much heavier than electrons, are not all swept out of the gap during one half cycle and begin to accumulate in the gap. To calculate this critical frequency, Eq. 2.14 is modified to account for the AC field and takes the form

$$v_{ion} = \mu E(1 - cos(\omega t)), \tag{2.21}$$

where ω is the angular frequency ($\omega=2\pi f$) and t is the time. The distance traveled by the ion in a given time may be attained by integrating with respect to t, which yields

$$d_{ion} = \mu E(t - \frac{sin(\omega t)}{\omega}). \tag{2.22}$$

The mobilities of O_2^+ in air [44] and N_2^+ in N_2 [45] with respect to E/N are retrieved from Viehland database in lxcat to make the necessary calculation. Note that the mobility of N_2^+ in N_2 is acceptable to use since 78% of air is composed of N_2. Assuming a 1 cm gap in atmospheric air, the DC breakdown field is approximately 30 kV/cm. The corresponding mobilities at 30 kV/cm are 2.558 $\frac{cm^2}{V \cdot s}$ for O_2^+ and 1.467 $\frac{cm^2}{V \cdot s}$ for N_2+. Using the lower mobility ion N_2^+ in Eq. 2.22, the critical frequency in which the ions begins to accumulate in the gap in one half cycle ($d_{ion} < 1\ cm$) is approximately 22 kHz.

Increasing the frequency higher than 22 kHz results in more positive ions getting trapped in the gap during one half cycle. The space charge created by the accumulation of positive ions enhances the electric field between the space charge and the anode electrode, see Fig.2.5. Consequently, this increases α in the gap and consequently lowers the effective breakdown field.
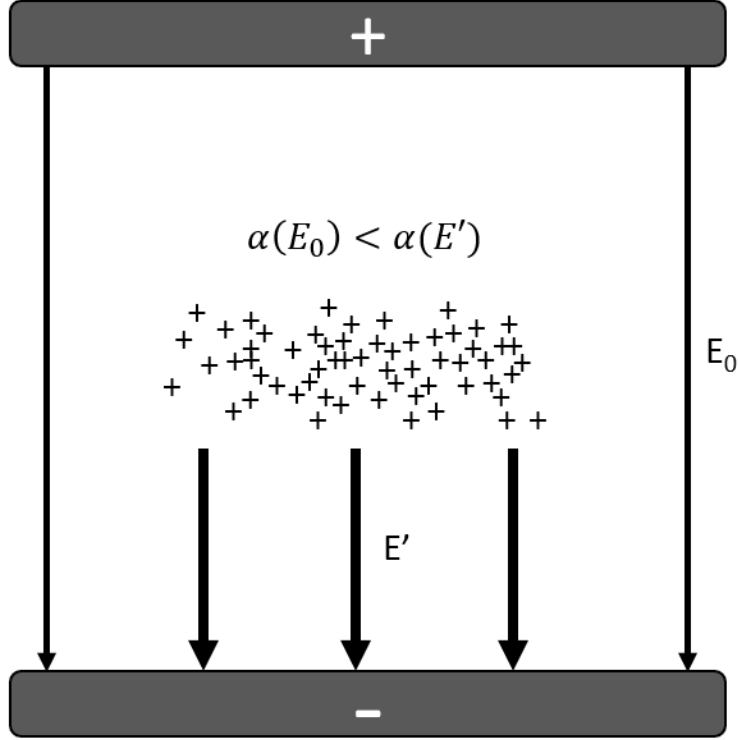
Figure 2.5. Positive ion space charge accumulation in a gap after several cycles. This assumes an RF field with sufficient magnitude and frequency. α is intensified due to the enhanced electric field between the space charge and the anode electrode.

At single digit MHz frequencies, this effect is at its peak, making the RF breakdown field approximately 80% of DC, see Fig. 12.3 in reference [1]. At a second critical frequency, RF breakdown field begins to rise due to the electrons starting to accumulate in the gap. Like for the first critical frequency pertaining to ion movement in the gap, a similar approach can be taken to calculate the critical frequency in which the electrons start to accumulate in the gap. The drift velocity of electrons with respect to E/N in atmospheric air is calculated using MultiBolt [7], which agrees well with tabulated data reported elsewhere (see Table 6.1 in [2]). Using the drift velocity in an RF field is written as

$$v_e(E) = v_{MB}(E) \cdot (1 - cos(\omega t)) \tag{2.23}$$

and the distance traveled for the electron is written as

$$d_e(E) = v_{MB}(E) \cdot (t - \frac{sin(\omega t)}{\omega}), \tag{2.24}$$

where $v_{MB}(E)$ is the drift velocity calculated by Multibolt as a function of the electric field. Assuming an RF field with a peak value of 24.5 kV/cm (80% of the DC breakdown field), the second critical frequency in which the electrons begin to accumulate in the gap during one half cycle starts $(d_e < 1\ cm)$ at approximately 6 MHz. Eq. 2.24 is graphed for several frequencies in the single digit MHz regime below, see Fig. 2.6.
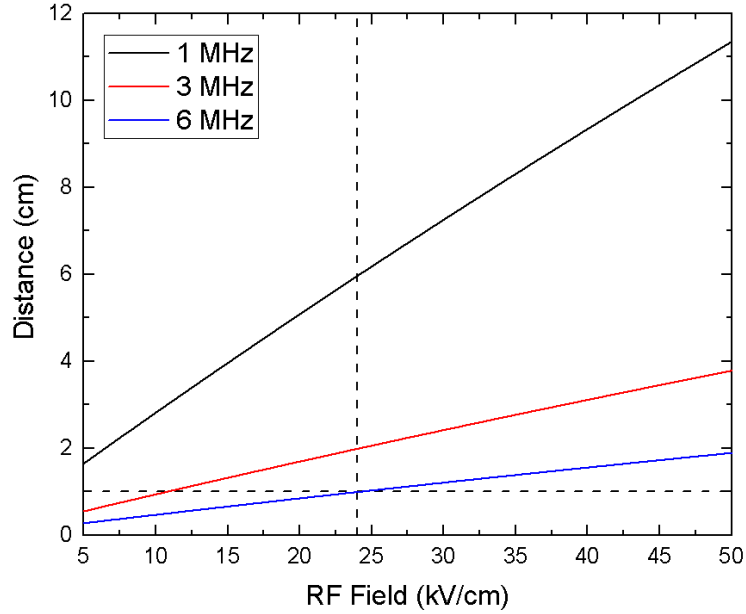
Figure 2.6. Electron distance traveled in one half cycle vs RF field for single digit MHz frequencies. Vertical dashed: 24 kV/cm (80% DC breakdown field); Horizontal dashed line: 1 cm. 6 MHz curve yields

As a point of comparison for the calculated critical frequencies, the relative breakdown field for atmospheric air as a ratio of RF to DC with respect to the frequency of the field is graphed below (Fig. 2.7) [10]. It is noted that the curves produced in Fig. 2.7 are corroborated by a Monte Carlo simulation where ion motion is neglected. The curve for the 1 cm gap is matches closely with the 1 cm curve reported in literature [1]. Therefore, Fig 2.7 is suitable to use as a point of comparison.
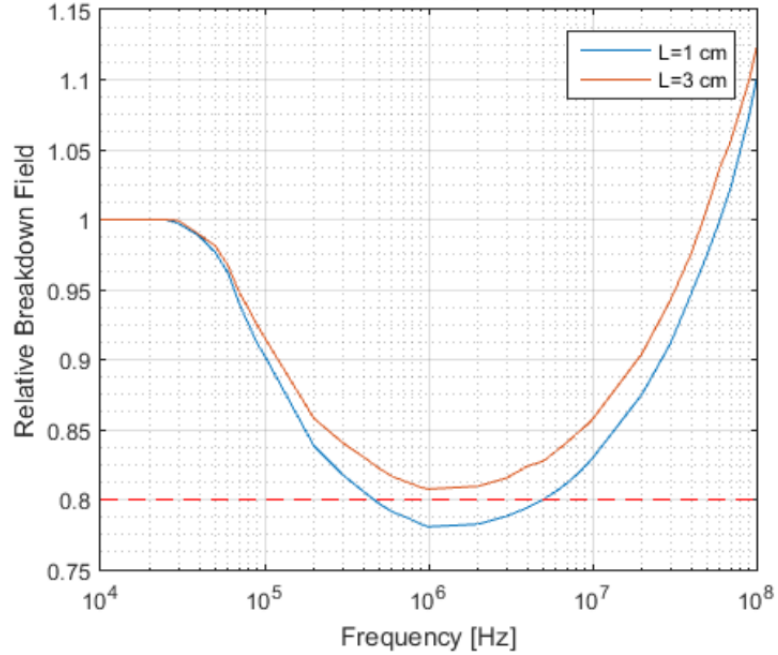
Figure 2.7. Simulated relative breakdown field as a ratio of RF to DC in atmospheric air for 1 (blue curve) and 3 (red curve) centimeter gaps [10]. The red dashed line marks a 0.8 (80%) relative breakdown field.

The relative breakdown field curve for a 1 cm gap begins to drop at approximately 25 kHz, which is close to the 22 kHz frequency calculated with Eq. 2.22. The lowest breakdown field (~ 80% of the DC field) occurs at 1 MHz. At frequencies beyond 1 MHz, the curve rises steadily. The second critical frequency that was calculated using Eq. 2.6 is off by a factor of 6. This is a result of the equation not considering other influencing factors to the electron movement such as the positive space charge in the gap. Nonetheless, the equation serves as a decent first estimate of the frequency at which electron mobility plays a role in affecting the relative RF breakdown field. At higher frequencies, the relative breakdown field exceeds the DC breakdown field. This rise in relative field due to the accumulation of electrons in the gap continues well into microwave frequencies, where the effective electric field is simply the rms field amplitude at frequencies as high as 30 GHz in atmospheric air [4].

2.4   Coronas

In non-uniform fields, the visual manifestation of locally confined ionization and excitation processes can be observed and measured well before breakdown between the electrodes occurs [1]. These manifestations are referred to as coronas. Coronas are undesirable in high power RF systems as they are a source of power loss and noise [32]. This discussion will focus primarily on coronas that form in a needle-plane gap (and similar geometries) since a protrusion in the high field region of the capacative plate gap is the geometry that is most likely to initiate corona in the ESA. The discussion begins with an overview on space charge effects and streamers. This is followed by coverage on coronas that form under static fields: anode directed and cathode directed coronas. For simplicity, they will be referred to as positive and negative needle corona here. Lastly, corona formation under alternating fields are discussed.

2.4.1   Space Charge Effects

When an electron avalanche takes place, it will generate a sufficient space charge as it traverses across the gap. The avalanche grows by $e^{\alpha x}$, where α is the ionization coefficient and x is the distance it travels. Positive ions are left behind by the electrons that are accelerating towards anode. The electrons and ions begin to separate and form a dipole, see Fig. 2.8 (a) [11]. While the electrons electrons are quickly absorbed by the anode, the heavy and slow ions remain in the gap, which accumulate and create a positive space charge. The positive space charge enhances the electric field on the cathode side of the configuration shown, see Fig. 2.8 (b).
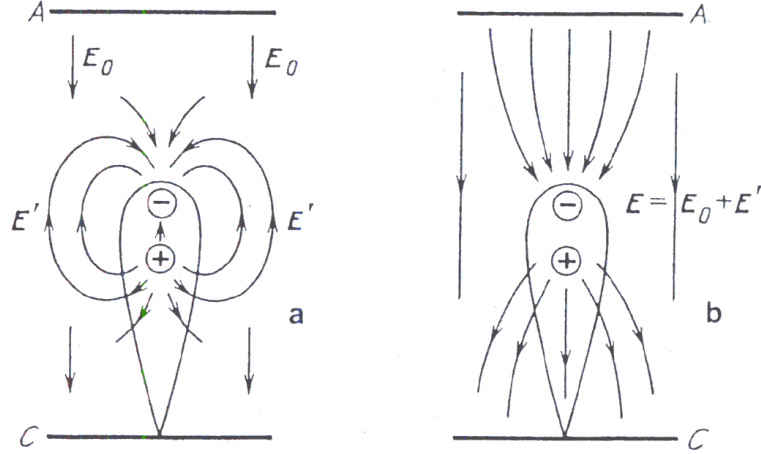
Figure 2.8. Electric field lines produced by an electron avalanche. (a) Field lines of space charge E' and externally applied field E_0 show separately. (b) The total field E as a summation of E'+E_0 [11].

2.4.2 Streamers

A streamer is a filamentary ionization channel that is vastly different from electron avalanches predicted by the Townsend mechanism [1]. They are formed by the primary avalanche in a sufficiently large electric field. Streamers may initiate from the anode or cathode in uniform fields over large gap distances or in asymmetric geometries at lower voltages. Once initiated, the streamer can distort the electric field upon reaching the electrodes, amplifying the current and eventually lead to breakdown of the gap [11]. This is referred to as the streamer breakdown mechanism. A single streamer propagating across the gap can be enough to initiate breakdown (in large gaps or when high overvoltage is applied).

To transition from the primary avalanche to a streamer, the avalanche must reach sufficiently high amplification and the space charge field must be on the same order of the applied electric field [11]. Otherwise, the avalanche will develop as it normally would.

In the case where the gap length and the overvoltage applied to the gap are not very large, the avalanche makes the transition to streamer at the point when it can no longer amplify, i.e., the avalanche reaches the anode [11]. The streamer is then

launched from the anode and propagates towards then cathode. This is referred to as a cathode directed streamer, see Fig. 2.9.
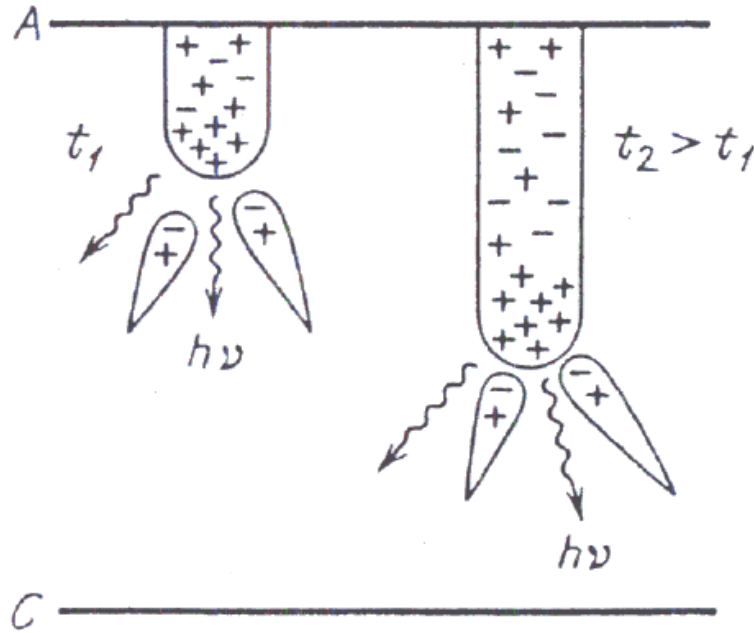
Figure 2.9. Development of cathode directed streamer at two different time intervals. Wavy arrows are photons with energy hν. [11].

It is suggested that the process of photoionization near the primary electron avalanche, which originates from photons generated by spontaneous emission of excited atoms in the electron avalanche, plays a critical role in the development of cathode directed streamers [11]. The electrons produced by photoionization give rise to secondary electron avalanches that move towards the anode due to the direction of the external field. These secondary avalanches intermix with the positive ions at front end of the streamer and create a quasineutral plasma. The secondary electron avalanches will also excite atoms and molecules, emitting new photons. Ions from the secondary electron avalanches make the streamer grow by enhancing the positive space charge portion of the plasma channel moving towards the cathode, attracting electrons for the next generation of secondary electron avalanches [11].

Given a sufficient generation of streamers, the gap will ultimately breakdown if the electron avalanches satisfy the Meek breakdown criterion [11], given by

$$\alpha(E_0)d \approx 18 - 20, N_e = exp(\alpha d) \sim 10^8, \tag{2.25}$$

where E_0 is the applied electric field, α is the ionization coefficient as function of E_0, d is the gap distance, and N_e is the number of electrons. For parallel plate gaps in atmospheric air, when d > 5 cm, the breakdown mechanism is streamer dominated [11]. At gaps less than 5 cm, breakdown occurs largely due to the Townsend mechanism.

In the case where the streamer is formed while the primary avalanche has not gone far from the cathode, it will develop primarily towards the cathode. This kind of streamer is referred to as an anode directed streamer, see Fig. 2.10.
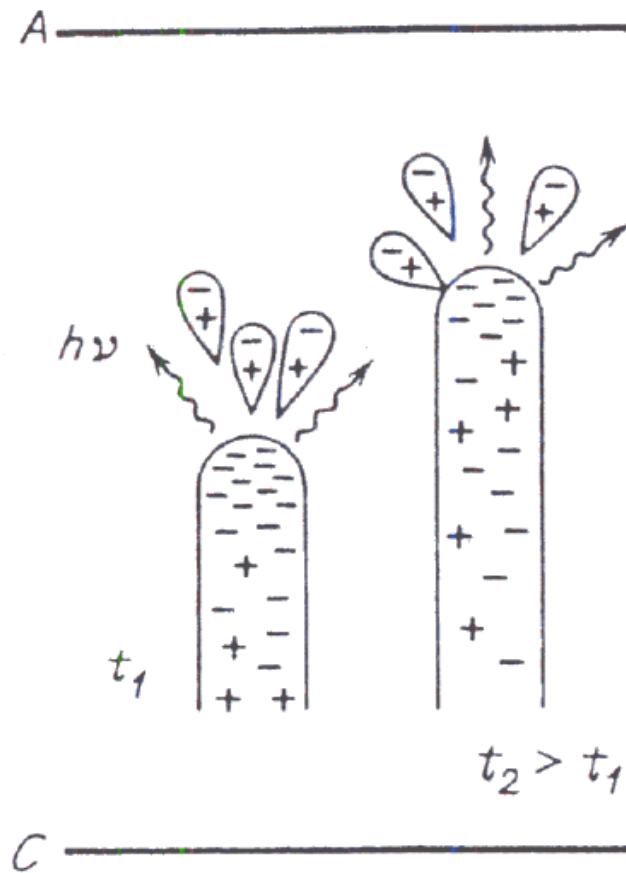
Figure 2.10. Development and propagation of an anode directed streamer at two different time intervals. Wavy arrows are photons with quantized energy hν. [11].

The mechanism for growth towards the cathode is the same as described for the

cathode directed streamer. However, the process for growth towards the anode is different. Secondary electron avalanches produced by photoionization develop in front of the negatively charged streamer head propagating towards the anode. The positive ions left behind by the secondary avalanches will intermix with the electrons in the streamer, in addition to the positive ions resulting from the primary avalanche, forming a quasineutral plasma.

2.4.3   Positive Needle Corona

In a needle-plane geometry, positive needle corona is a corona that forms on the needle when its voltage is positive in reference to the plane electrode. Voltage applied to this electrode configuration will produce a non-uniform field where the field stress is highest at the tip of the needle. The first ionizing event that manifests when a sufficient voltage is reached takes the form of a streamer [1]. Under a steady field, these streamers develop with varying frequencies. The streamers here are short due to natural statistical fluctuations and are referred to as burst pulses [1]. As the applied voltage is increased further, the frequency of the streamers increases until all transient behavior ceases and a thin glow will manifest along the tip of the positive needle [1]. The glow will become more intense and luminous with increasing voltage. At a certain point, the glow discharge ceases and transitions back to streamers. However, these streamers are more intense and are a source of acoustic noise. They are referred to as breakdown streamers, since they can lead to complete breakdown of the needle-plane gap. To aid in the visualization of the transitions for the different manifestations that form in positive corona, a graph showing the threshold curves for these manifestations in a rod-plane gap is presented below, see Fig. 2.11 [12].
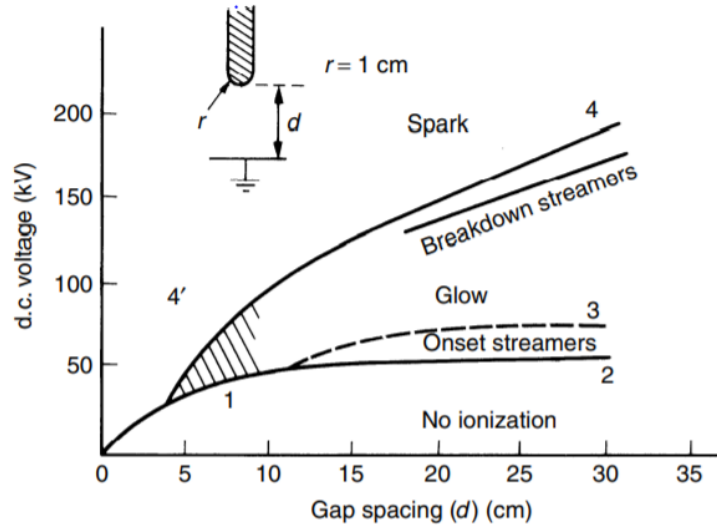
Figure 2.11. Threshold curves for various modes of positive corona in a rod-plane gap with a rod radius of 1 cm [12].

2.4.4   Negative Needle Corona

Negative needle corona forms when the needle voltage is negative relative to the plane electrode. When voltage is applied to the gap and is slowly increased, currents of the order of 10^{-14} A are measured [1]. No ionization is occurring at these current levels. Once a certain voltage is reached, the current will rise significantly and a form of ionization that produces consistent current pulses takes shape [1]. These manifestations have been studied extensively by Trichel in 1938 and are thus named Trichel pulses. The Trichel pulses may reach a frequency of a few 10^6 pulses per second before transitioning to a stable glow discharge [1]. At a higher critical voltage, the onset of negative streamers occurs. These negative streamers are unstable at smaller gap sizes and will consequently lead to complete breakdown of the gap after the initial streamer. The threshold curves for different manifestations of corona in a negative rod-plane gap are graphed below, cf. Fig. 2.12 [12].
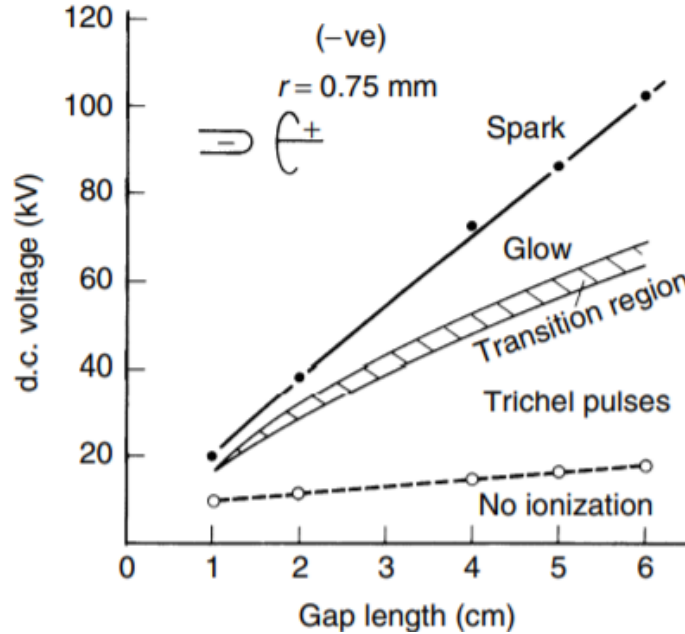
Figure 2.12. Threshold curves for various modes of negative corona in a rod-plane gap with rod radius of 1 cm [12].

2.4.5 Corona Under Alternating Fields

The behavior of corona under alternating fields largely depends on the frequency of the field. At power frequencies (50-60 Hz), the field reversals in the needle-plane gap is not fast enough to inhibit the movement of ions or electrons across the gap in atmospheric air. Therefore, the corona will form similarly to the those under the DC field. The manifestations of positive and negative needle corona present themselves under the alternating field. At a high enough applied voltage, the needle-plane gap will breakdown with preference of breaking down during the positive half cycle, see Fig. 2.13 [1]. This is a consequence of the breakdown voltage for the positive needle being lower than the negative needle. This behavior observed at low frequencies (50 Hz) appears to not present itself for 3.3 MHz breakdown in a needle-plane gap; the distinction between the onset of breakdown occurring on the positive or negative needle cannot be clearly made (see section 4.4).
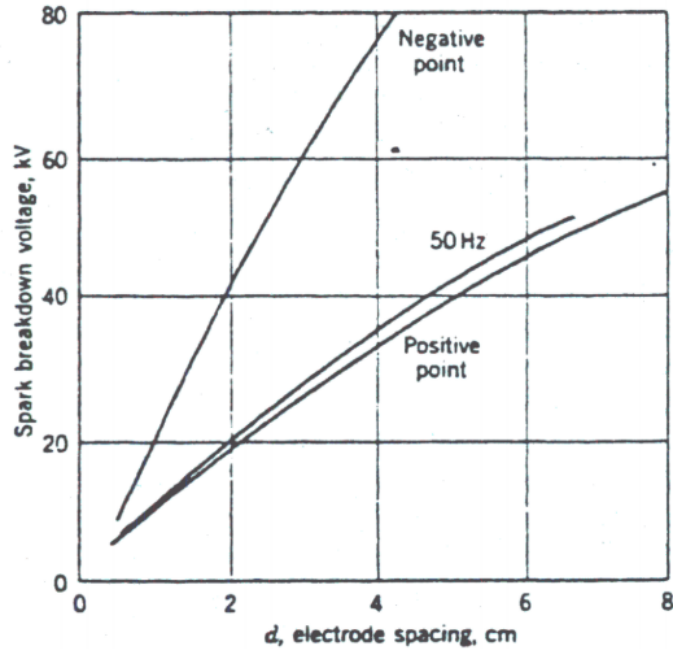
Figure 2.13. Breakdown voltage comparison of negative needle, positive needle, and 50 Hz in a needle-plane geometry. Needle radius is less than 0.01 mm [1].

As the frequency is increased, the onset voltage of the corona begins to decrease. It decreases 3-5% at 10^5 Hz [1] and roughly 15% at 10^6 Hz [13]. The current that is drawn in high frequency corona is also larger than corona at lower frequencies and static fields. At high frequencies, electrons and ions do not cross the gap freely. Instead, they oscillate in the gap and accumulate over many cycles, giving rise to higher currents. The breakdown voltage of high frequency corona is considerably lower than reported for low frequency corona. Between 50 Hz and 75 kHz for a needle-plane geometry, the difference in breakdown voltage dropped by 55%, see Fig. 2.14 [13].
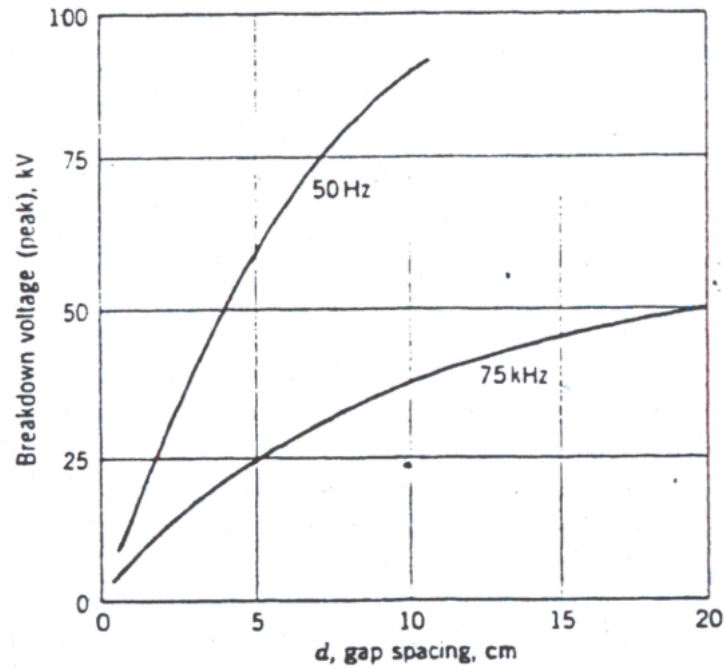
Figure 2.14. Breakdown voltages for 50 Hz and 75 kHz corona in a needle-plane gap [13].

2.5   RF Breakdown Test Setup

2.5.1   Resonant Circuits and Quality Factor, Q

A resonant circuit may be modeled by a series or parallel RLC lumped-element equivalent. A circuit model of the series and parallel resonant circuits are depicted below, see Fig 2.15.
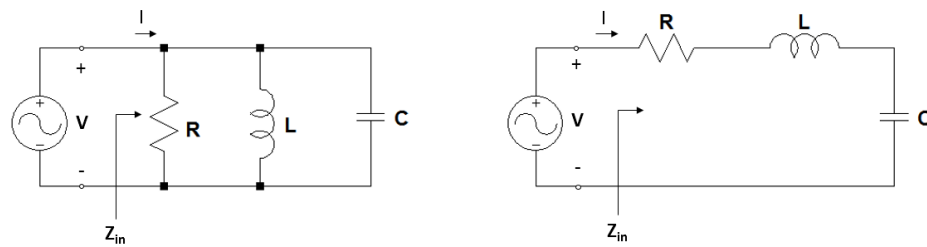
Figure 2.15. Parallel (left) and series (right) resonant circuits.

A circuit is said to be in resonance when the average stored magnetic energy in the inductor, W_m, and the average stored electric energy in the capacitor, W_e are

33

equal. One finds the resonant frequency for both series and parallel resonant circuits when R (damping) can be ignored as

$$\omega_0 = \frac{1}{\sqrt{LC}}. \tag{2.26}$$

For completeness, the equations for input impedance, power loss, and stored magnetic energy from literature are tabulated below, see Table 2.3. One may find the derivations of the tabulated equations in detail in literature [3].

Table 2.3. Equations for series and parallel resonators [3].

Quantity	Series Resonator	Parallel Resonator
Input impedance/admittance	$Z_{in} = R + j\omega L - j\dfrac{1}{\omega C}$	$Y_{in} = \dfrac{1}{R} + j\omega C - j\dfrac{1}{\omega L}$
Power Loss	$P_{loss} = \dfrac{1}{2}|I|^2 R$	$P_{loss} = \dfrac{1}{2}\dfrac{|V|^2}{R}$
Stored magnetic energy	$W_m = \dfrac{1}{4}|I|^2 L$	$W_m = \dfrac{1}{4}|V|^2 \dfrac{1}{\omega^2 L}$
Stored electric energy	$W_e = \dfrac{1}{4}|I|^2 \dfrac{1}{\omega^2 C}$	$W_e = \dfrac{1}{4}|V|^2 C$

The quality factor, Q, is a measure of the power loss in a resonant circuit. A high Q indicates low loss in the circuit. Losses in resonant circuits can come from conductor loss, dielectric loss, or radiative loss. The loss can be represented by the resistance R in the equivalent circuit. Connecting an external circuit to the resonant circuit may introduce additional loss, which will lower the Q. The Q of the resonant circuit itself without loading effects is unloaded Q, denoted as Q_0. The unloaded Q is given as

$$Q_0 = \frac{1}{\omega_0 R C} \tag{2.27}$$

for series resonant circuits and

$$Q_0 = \omega_0 R C \tag{2.28}$$

for parallel resonant circuits.

In practical applications, the resonant circuit is connected to external circuitry, which will impact the overall Q, or loaded Q, Q_L of the circuit. Fig. 2.16 depicts a resonant circuit connected to an external load resistor, R_L.
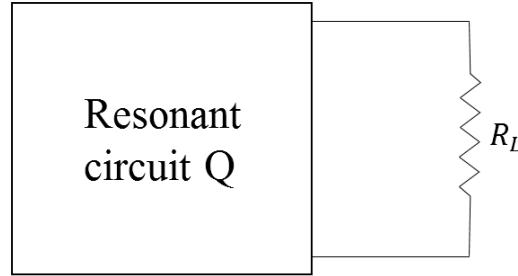
Figure 2.16. Resonant circuit connected to external load R_L

In the case of an external load resistor being connected, the effective resistance of the series resonant circuit becomes R + R_L. The external load resistor is in parallel with the parallel resonant circuit, so the effective resistance becomes RR_L/(R+R_L). If the external Q, Q_e is defined as

$$Q_e = \frac{\omega_0 L}{R_L} \tag{2.29}$$

for series circuits and

$$Q_e = \frac{R_L}{\omega_0 L} \tag{2.30}$$

for parallel circuits, then the loaded Q can be expressed as

$$\frac{1}{Q_L} = \frac{1}{Q_e} + \frac{1}{Q_0}. \tag{2.31}$$

2.5.2 Skin Effect

The skin effect is the tendency of alternating current to distribute itself in a conductor in such a way that the current density is largest towards the surface and decreases exponentially deeper into the conductor. The current will flow mainly

between the outside of the conductor surface and down to a certain level, regarded as the skin depth. The skin effect is the consequence of opposing eddy currents that are induced by changing magnetic field created by the AC current. The skin depth is commonly written as

$$\delta = \sqrt{\frac{2\rho}{\omega\mu}} \tag{2.32}$$

where ρ is the resistivity of the conductor, ω is the angular frequency of the current, and μ is the permeability of the conductor μ_r μ_0. As the frequency increases, the skin depth decreases.

The most significant effect created by the skin effect is the increase of a wire's effective resistance and resulting losses. The effective resistance, R, due to a current being restricted to the surface to a large conductor (diameter D $>>$ ρ) of length L can be found by

$$R \approx \frac{L\rho}{\pi(D - \delta)\delta} \approx \frac{L\rho}{\pi D \delta}. \tag{2.33}$$

Note that this equation is only accurate for an isolated wire. For the case of nearby wires like seen in a cable or coil, the effective resistance under AC excitation is also effected by the proximity effect, which adds to the overall effective resistance.

2.5.3 Proximity Effect

Given two conductors within close proximity with AC current flowing, the current density will will not only distribute itself towards the outer edges of the conductor (due to skin effect), but also crowd in certain spots. This crowding phenomenon is a result of the proximity effect. An example of the proximity effect for two conductors with their respective flowing in the same direction is shown below, see Fig. 2.17. Note that if the currents are flowing in the opposite direction of each other, the current density will crowd towards the center between the two conductors.
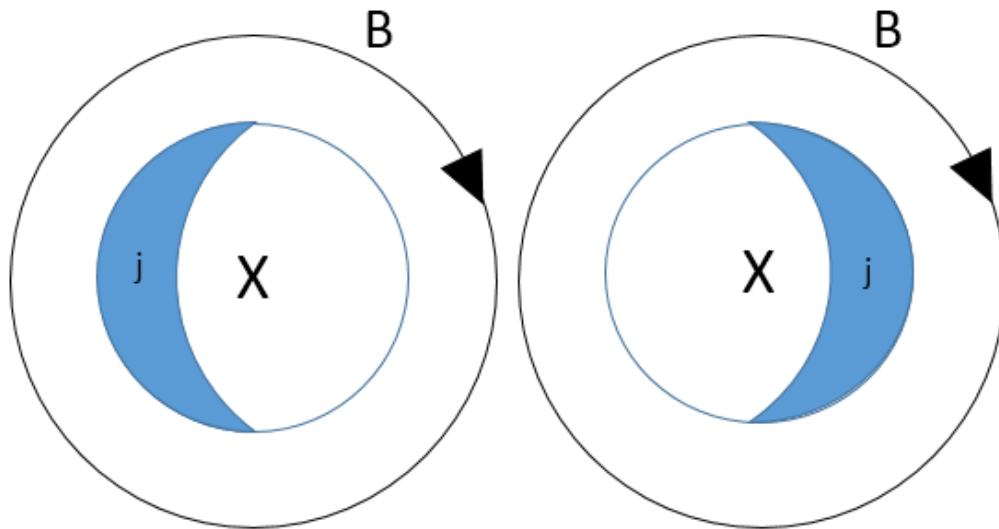
Figure 2.17. Proximity effect for two conductors where the currents are going in the same direction (x-into the page). The current density, j is crowding away from the center between the two conductors.

The current crowding from the proximity effect increases the effective resistance of the circuit with increasing frequency, which can be problematic in designing low loss components. The resistance due to the proximity effect can be minimized by increasing the spacing between two current carrying conductors. However, the resistance due to the skin effect cannot be avoided since it is frequency dependent.

2.5.4   Scattering Parameters

Scattering parameters (S parameters) are a useful design aid for RF engineering. S parameters use normalized incident and reflected waves to describe the properties of complex networks as a simple black box [46]. Given an RF signal that enters an incident port, some fraction of the signal may be reflected back to the incident port. Some parts of it may also scatter to other ports, getting attenuated or amplified in the process. For analysis, we refer to the 2-port network, see Fig. 2.18.
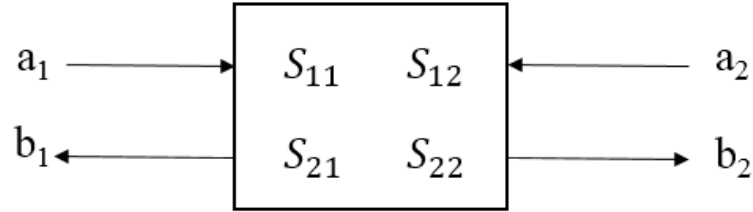
Figure 2.18. Generalized 2 port network with a characteristic impedance Z_0. The variables a and b are voltage like variables.

The first number of in the subscript of the S parameter refers to the responding port and the second number refers to the incident port. The S_{11} is a measure of the reflected power at the input of a network. Often, it is termed as the reflection coefficient. The S_{21} can be referred to as the gain or insertion loss, the S_{12} is the reverse isolation, and the S_{22} is the output reflection coefficient. When both ports are terminated in reference to Z_0, the S parameters of a 2 port network may be defined as

$$S_{11} = b_1/a_1$$
$$S_{12} = b_1/a_2$$
$$S_{21} = b_2/a_1$$
$$S_{22} = b_2/a_2$$

S parameters are complex numbers, since both the magnitude and phase of the signal is altered by the network. In the application of measuring S parameters of the RF setup used in the breakdown/corona experiments, we care only about the magnitude portion of the S parameters, since the effect of the phase is does not need to be known.

CHAPTER 3

EXPERIMENTAL SETUP

It is desired to study DC and 3.3 MHz RF breakdown/corona in atmospheric conditions. To accomplish this task, an experimental setup, which is fed with a high voltage DC source or with an RF source capable of generating sufficiently high RF voltages, is needed. The discussion begins with the preparation of the electrodes used in the breakdown and corona experiments. Finally, the DC and RF setups, which vary to some degree depending on the experiment being performed, are presented in detail.

3.1   Electrode Preparation

Bruce profile [47] electrodes composed of 360 machinable brass and 304 stainless steel were machined. In addition, 1.9 cm spherical electrodes made of 360 machinable brass were made. The machined electrodes are then smoothed in multiple sanding steps using sand paper with decreasing grit size. After sanding the electrodes with 2000 grit sand paper, they are polished to a mirror finish. This is done to prevent surface roughness from affecting the breakdown voltage measurements. The brass electrodes are polished with TC6 Emery E5 followed by white Rouge WR1 compound. The stainless steel electrodes are polished with Jewelers Rouge JR1 followed by white Rouge WR1 compound. The electrodes are cleaned with a Kimwipe soaked in Acetone to remove residual polishing compound from the surface. The Bruce profile electrodes and spherical electrodes are shown together in Fig. 3.1.

Figure 3.1. Brass and stainless steel Brass electrodes and brass spherical electrodes used in breakdown experiments.

The dimensions of the Bruce profile electrode are given in the schematic below, see Fig. 3.2.
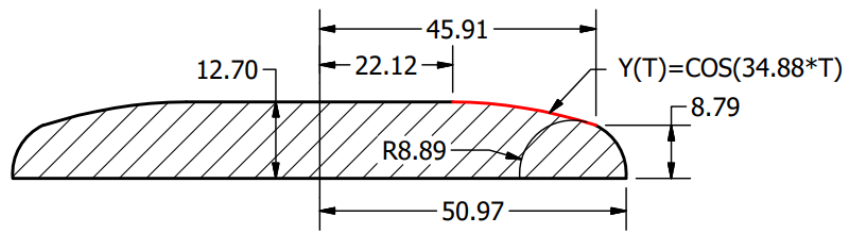
Figure 3.2. Bruce profile electrode schematic. T represents the independent axis variable and dimensions are given in millimeters. [4].

The spherical electrodes were selected to replicate Friedrich Paschen's famous breakdown experiment [41] in which he measured the DC breakdown voltage of spherical brass electrodes at various gap distances. Bruce profile electrodes were selected and used in both DC and RF breakdown experiments because their geometry minimizes edge effects and forms a homogeneous field around the center of the electrode gap. A field simulation of a Bruce profile electrode pair showing a uniform field at

the center of the gap is shown in Fig. 3.3. With a homogeneous gap and reduced edge effects, the measurement of the true breakdown voltage of the gap can be ensured.
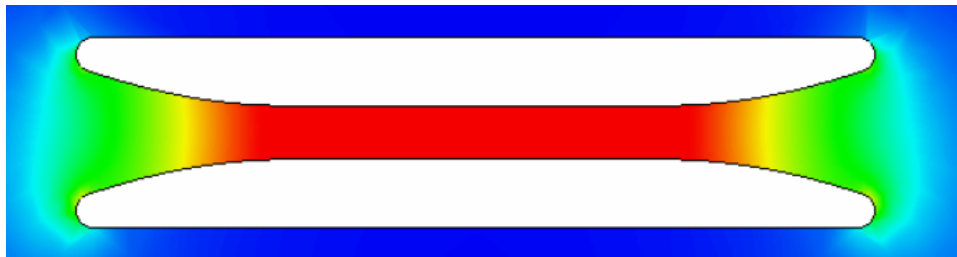
Figure 3.3. Electric field simulation of Bruce profile electrode pair [14]

Various needle electrodes were employed for the corona experiments. For the initial corona experiments, a machined tungsten needle was used, see Fig. 3.4. The machined tungsten needle has a 47.6 mm tapered length, a 250 μm tip radius, and a 6.36 mm base width.

Figure 3.4. Machined tungsten needle used in initial DC and RF corona experiments.

Two pure tungsten electrodes of 3.2 mm diameter and 87 mm in length were sharpened with different included angles as well, see Fig. 3.15. The taper angles of the pure

tungsten electrodes are 31.4° and 44.2 °. These electrodes were sharpened at different angles study the effect of the different included angles on the IV characteristics for positive and negative needle corona.
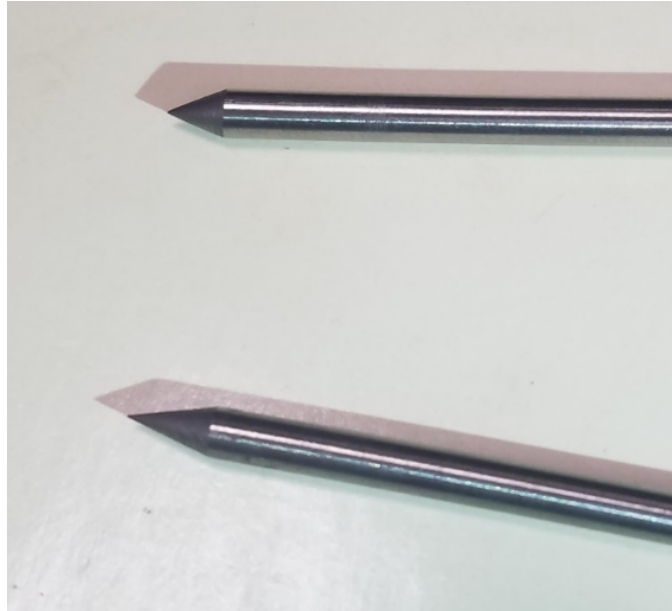
Figure 3.5. Pure tungsten needle electrodes with 31.4°and 44.2°included angles.

Finally, three pure tungsten needles and three 2% lanthanated tungsten needles of the same length and diameter as described for the earlier set of pure tungsten needles were used. The pure tungsten and lanthanated tungsten needles were sharpened at the same angle. To accomplish this, the electrodes were fitted into an electric screwdriver and rotated slowly as they were sharpened to try to get the needle geometry as symmetric as possible. The order in which the electrodes were sharpened alternated by material. A pure tungsten was sharpened first, followed by lanthanated tungsten, and then back to a pure tungsten electrode. This method of sharpening was repeated until all 6 needles were sharpened. The electrodes were numbered 1-6 by the order in which they were sharpened. The naming convention is given by the material (P for pure tungsten or L for lanthanated) followed by the number. Photos of the electrode tip geometries were taken before and after RF voltage application to analyze the differences in tip geometry after having gone through numerous corona

ignitions. Two markings 90° apart from each other were made at the base of each electrode to differentiate between the two sides of the electrode tip geometry that were photographed.
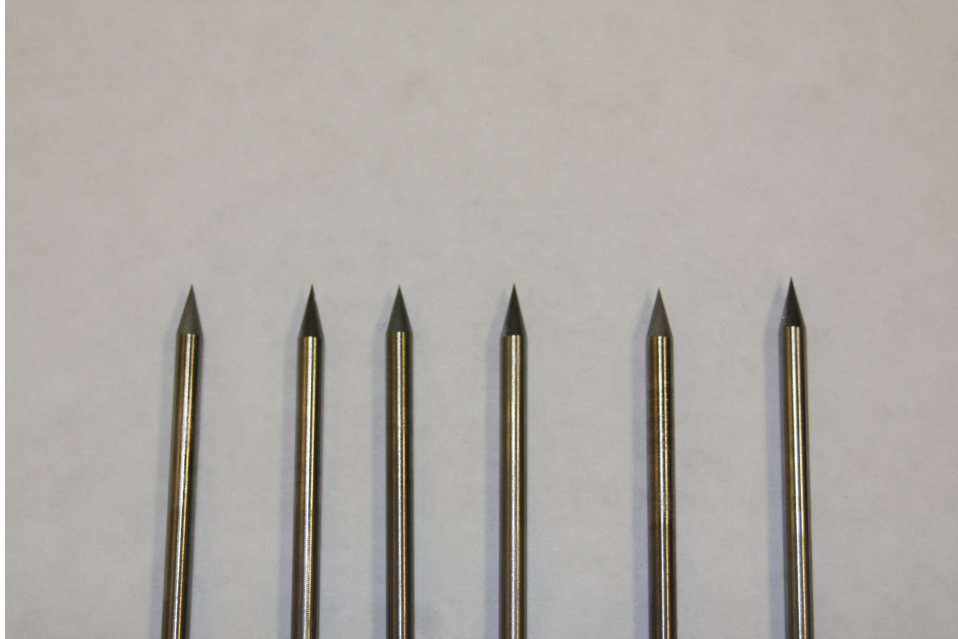
Figure 3.6. Machined tungsten needle used in initial DC and RF corona experiments [5].

3.2 DC Breakdown Setup

A high potential tester is connected to the electrode gap to supply the DC voltage, see Fig. 3.7. The voltage of the high potential tester is slowly increased by hand until breakdown occurs. The gap voltage at the point of breakdown is directly measured with a 1000:1 commercial high voltage probe. DC breakdown measurements are observed for 1-10 mm gaps.

Figure 3.7. Gap setup for DC breakdown. A high potential tester and a commercial high voltage probe are connected to the top electrode while the bottom electrode is connected to ground. The electrode configuration shown is two brass Bruce profile electrodes separated by a 1 cm gap [4].

3.3   RF Breakdown Setup

The RF setup utilizes the same electrode setup, but the high potential tester is replaced with a custom made high voltage RF source. A highly resonant loosely coupled LC tank was constructed to generate tens of kilovolts at MHz frequencies. The RF source itself consists of a signal generator connected to a series of amplifiers to produce a maximum of 1500 W output to the load (being the LC tank circuit). The RF source signal path is depicted in Fig. 3.8.
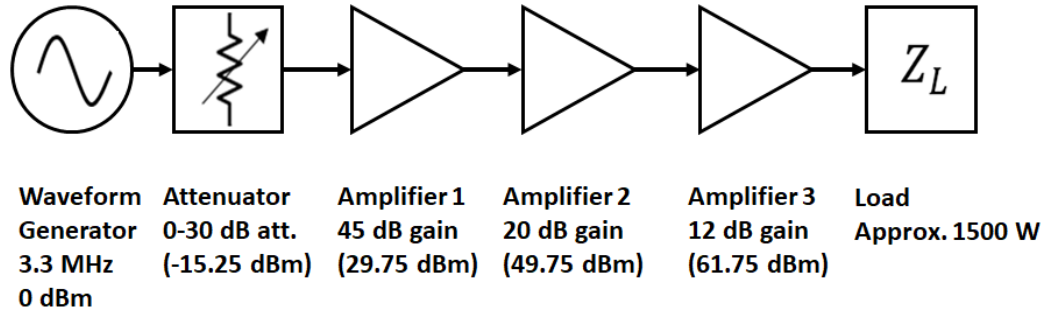
Figure 3.8. Simplified block diagram of RF source signal path. Attenuation and usage of amplifiers is varied depending on the experiment. Total gain from amplification: 77 dB. The output of Amplifier 3 is limited to 1500 W. [4].

The coil L2 is a rather large structure in contrast with the rest of the circuit due to the resistive losses in smaller coils, see Fig. 3.9. The geometry of coil L2 is of a square design, where the diameter of the coil is approximately equal to its length. It is designed this way to minimize loss and maximize the quality factor, Q. Both coils are constructed with 9.5 mm diameter malleable copper tubing. The low resistivity of the copper tubing in addition to its large conductor surface yielded low Ohmic resistance at MHz frequencies. The total resistance of coil L2 was estimated to be approximately 1.5 Ohms. Factoring in the calculated resistance due to the skin effect and the DC resistance, 212 mOhms and 5 mOhms respectively, the remaining resistance due to proximity effect is 1.283 Ohms. The dimensions of L2 are 25.4 cm x 24.13 cm with 14 turns. The primary coil, L1, is 3.6 cm x 12.68 cm with 3 turns. A variable vacuum capacitor is connected in parallel with the electrode gap to tune the circuit to the desired resonant frequency. A frequency of 3.3 MHz was selected for the entirety of the RF experiments. The resonant frequency, in addition to the S11 (reflection coefficient) and Q of the circuit are verified with a network analyzer. A low coupling coefficient of k ~ 0.1 is necessary for this circuit to achieve the high Q needed to generate sufficiently large RF voltages. Therefore, the placement of coils L1 with respect to L2 is critical within 0.5 mm in length. Any positional shifting of L1 beyond 0.5 mm will alter the Q and S11 to the point where the maximum achievable RF voltage is reduced.
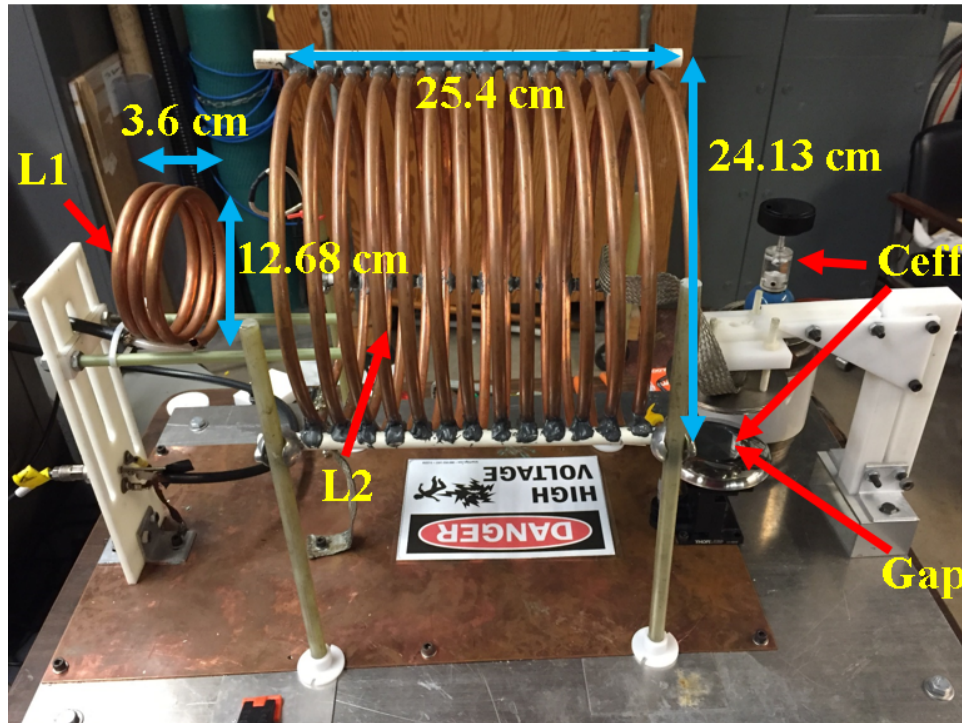
Figure 3.9. Physical setup for RF breakdown and corona experiments with coil dimensions. L1 – primary inductance; L2 – secondary inductance; Ceff – effective capacitance consisting of electrode gap in parallel with a tuning capacitor [4].

For 400 W on input RF power, the resonator circuit produces an output voltage of +/- 30 kV (60 kV peak-to-peak) across the gap. Carefully tuning the mutual inductance of the LC tank circuit makes it appear as a 50 Ohm load to the RF source. A simplified circuit of the RF setup is depicted in Fig. 3.10.
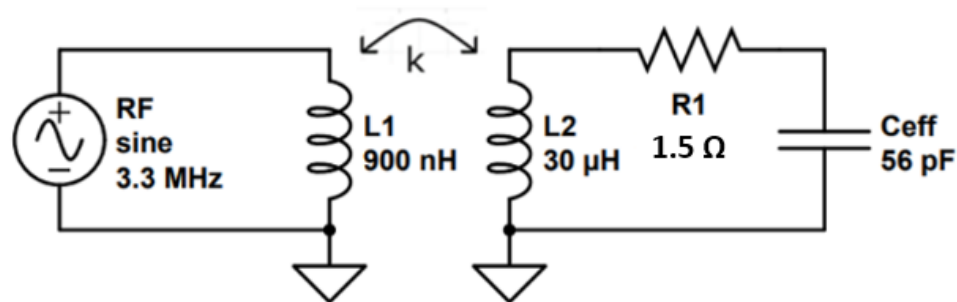
Figure 3.10. Simplified schematic of highly resonant loosely coupled LC circuit. 50 Ohm impedance; L1- primary inductance; L2-secondary inductance; Ceff - effective capacitance, gap and tuning capacitor; R1 – total resistance of coil L2; k – coupling coefficient ~ 0.1

3.3.1 Capacitive voltage divider

The RF voltage is monitored through a custom made capacitive voltage divider, see Fig. 3.11. A 2 nF parallel plate capacitor was built and connected in series with the variable vacuum capacitor to create the voltage divider between C2 and C3. The parallel plate capacitor is made with two 10 cm diameter brass plates with 0.051 mm Kapton film as the dielectric material between the plates. It is important to make sure that the surface of the brass plates are smooth and clean. Otherwise, the rough surface can puncture the thin Kapton film and short the capacitor. The RF voltage is measured at the node Vout with a 100:1 probe and fed into an oscilloscope. To prevent breakdown from occurring at the edges of the capacitor when the RF voltage is pushed towards its upper limit, the sides are coated with super corona dope, which is rated to hold off up to 1.614 x 10^3 kV/cm.
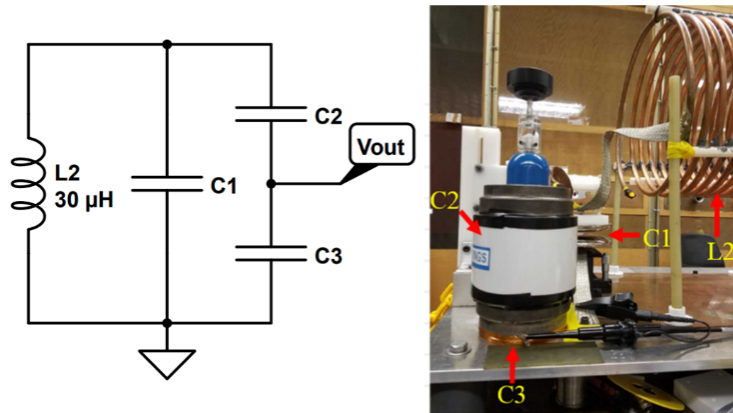
Figure 3.11. Gap setup for DC breakdown. A high potential tester and a commercial high voltage probe are connected to the anode electrode [4].

3.3.2 RF Excitation Methods

The RF setup is fed by three different excitation methods at 3.3 MHz. The first excitation method consists of a continuous wave RF signal with a slowly rising voltage, which is achieved by slowly decreasing the attenuation of the signal by hand until breakdown occurs. The RF envelope increases at rate of ~ 5 mV/μs.

The second excitation method is a fast rise pulse that lasts for 5000 cycles, see Fig. 3.12. The rise time of the envelope is typically around 200 V/μs. It is noted that amplifier 3 in the RF source signal path is not used in this excitation method, cf. Fig. 3.8.
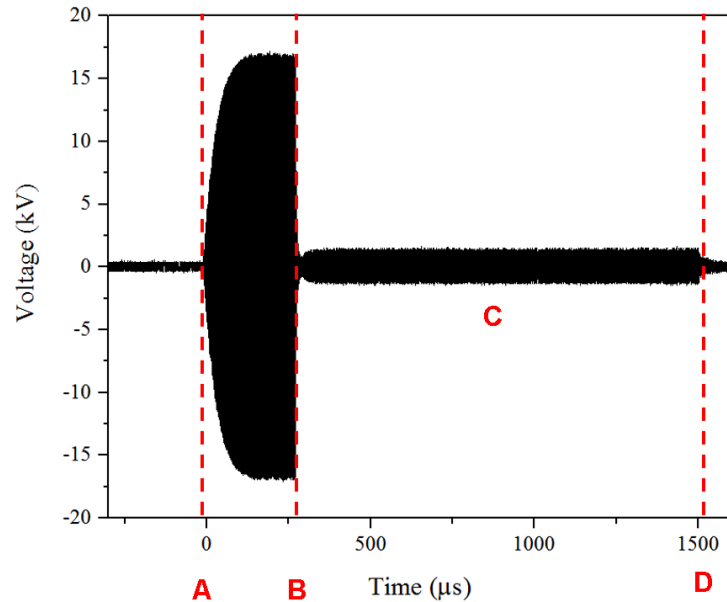
Figure 3.12. Fast rise RF breakdown waveform. The pulse signal is 5000 cycles at 3.3 MHz. (A) RF signal on. (A) and (B) ring up. (C) breakdown and plasma arc. (D) RF signal off. [4].

For the third excitation method, amplifier 3 is switched on with the same pulse conditions, yielding an envelope with a steeper rise as high as 1400 V/μs, cf. Fig. 3.13. Typically it takes no more than 30-40 cycles to breakdown gaps less than 5 mm when this type of excitation is applied.
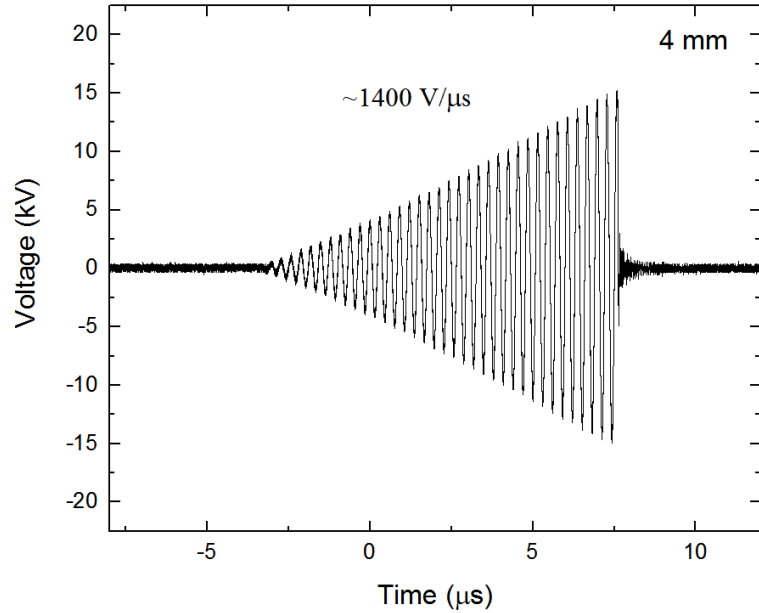
Figure 3.13. Faster rise RF waveform measured for stainless steel Bruce profile electrodes spaced 4 mm apart. The rise time of the envelope is approximately 1400 V/μs.

3.3.3 RF Setup and UV Application

To study the effects of seeding electrons in the electrode gap under faster-rise RF excitation, an external UV source was implemented into the RF setup. The UV source was Spectra Physics xenon flash lamp. The radiated light from the lamp was measured with a spectrograph to validate its capability of generating UV photons with high enough energy induce photoemission on stainless steel electrode surfaces, cf. Fig. 3.14. The spectrograph yielded peaks at 246.67 nm and 259.73 nm, which translate to higher energies than the 4.34 eV work function of 304 stainless steel that is reported elsewhere [48]. Therefore, the lamp was confirmed to be a sufficient source to seed electrons in the gap. It is noted that the spectrum was not corrected for the spectral sensitivity of the detector, hence the lower peaks seen in deep UV range.
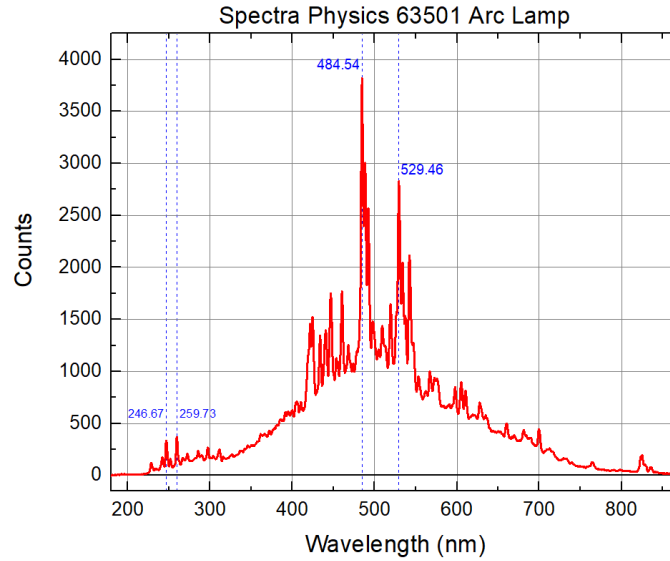
Figure 3.14. Spectrograph of Spectra Physics Xenon flash lamp. The highest peaks were measured at 484.54 nm and 529.48 nm. Deep UV peaks were found at 246.67 nm and 259.73 nm. [4]

A calcium-fluoride plano-convex lens was placed between the UV source and the electrode gap. CaF_2 has better transmission at the deep UV range than other materials such as fused silica. The image produced by the lens was directed into the electrode gap so that the UV irradiates both electrodes.
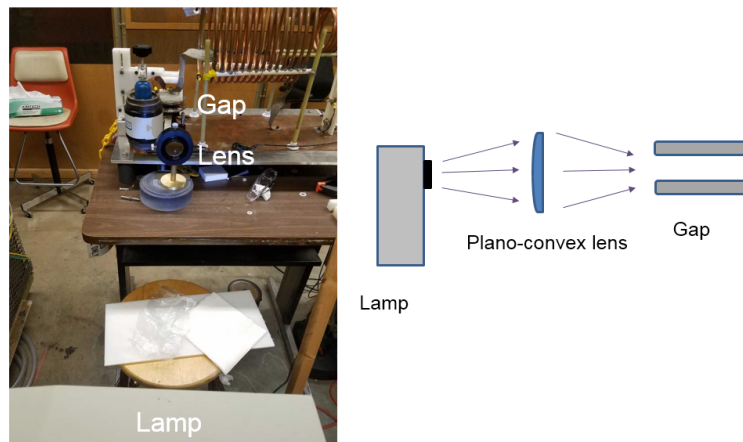
Figure 3.15. RF setup for UV application. The UV source (lamp) is in line with the electrode gap. A UV clear plano-convex is placed between the source and electrode gap to direct the light into the gap.

3.3.4   RF Setup with ICCD Camera

There was interest in imaging the ionization activity that takes place a few tens of nanoseconds before RF breakdown is initiated to compare with physical assumptions made for a PIC Monte Carlo simulation for that calculates the RF breakdown field while including photon processes. To image the prebreakdown activity, an ICCD camera was used. A diagram of the setup is shown in Fig. 3.16. Since the simulation assumes an excess of electrons in the gap, a highly pure UV LED source that produces light centered at 275 nm (bandwidth ~ 10 nm) was used to seed electrons in the gap. A UG11 filter with 80% optical transmission between 275-375 nm was placed in front of the optical window of the ICCD camera to attenuate visible light and pass UV light.
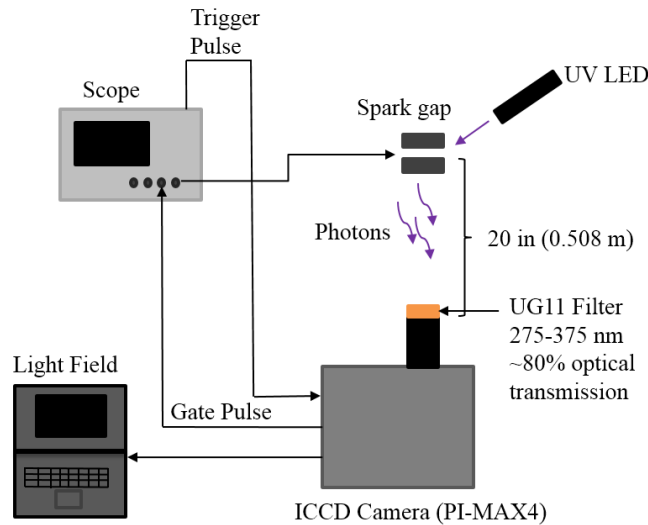
Figure 3.16. RF setup with ICCD camera to image RF prebreakdown in the electrode gap. The parameters of the ICCD camera (gain, gating time delay, and gate pulse with) are modified using an laptop running LightField. The gate pulse of the ICCD is fed back into the oscilloscope to see when the camera was gated on with respect to the RF voltage signal.

The ICCD camera used in the experiment was a PI-MAX 4 made by Princeton Instruments. The PIMAX4 ICCD camera utilizes a RB Fast Gate photocathode, which is a gen II photacathode that can be gated down to 2 ns. The QE of the RF

fast gate photocathode floats between 10-15% for 275-375 nm photons. An overview on how the ICCD camera works is covered in Appendix A.

The RF voltage applied to the gap is amplified by all three amplifiers in the RF setup to produce a waveform with as sharp as a rise time as possible, cf. Fig 3.8. An example of one the the wave forms that was produced with the implementation of the three amplifiers is shown earlier, see Fig. 3.13. The ICCD camera gate is externally triggered by the scope output, which triggers off the measured RF voltage. The corresponding gate signal pulse is fed back to the oscilloscope to observe when the camera was gated with respect to the applied RF signal. To set the gate width, delay, and gain for the experiment, the RF voltage is applied and the camera parameters are adjusted until they were optimal for capturing the prebreakdown event.

3.4 Corona Setup

A stainless steel Bruce profile electrode and a tungsten needle electrode are arranged in a needle-plane geometry for corona measurements, see Fig 3.17. The needle electrode is grounded while DC or RF voltage is fed to the plane electrode.
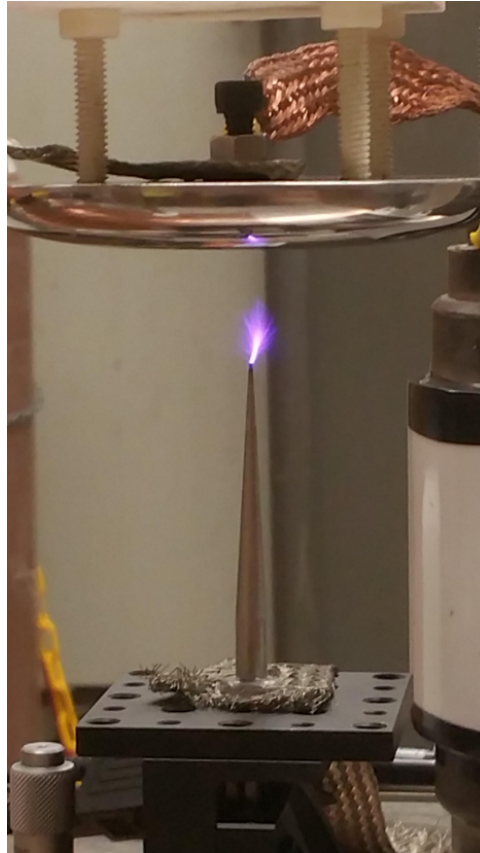
Figure 3.17. Stainless steel Bruce profile electrode and machined tungsten needle arranged in needle-plane geometry for corona experiments. RF Corona is ignited at 3.3 MHz in a 2 cm gap. [4].

3.4.1 DC Corona Setup

In order to produce positive and negative corona, two different high potential testers of opposite polarity were utilized. Positive corona was generated by applying negative voltage to the plane electrode while negative corona was generated by applying positive voltage to the plane electrode. Voltage was increased at 1 kV increments and both the time averaged current and voltage displayed on the high potential tester were recorded. The machined tungsten needle electrode and two pure tungsten electrodes with different included angles were used in the DC corona setup. The gap spacing was set to 2 cm.

3.4.2   RF Corona Setup

Two different setups were implemented to measure and study RF corona. In the first setup, a digital watt meter was placed between the output of the amplifier chain and the load to measure the forward power being delivered to the needle-plane gap, cf. Fig. 3.8 [4]. The input power is increased peak RF voltage with respect to the forward power was recorded. The machined tungsten needle spaced 2 cm apart from the plane electrode was used for RF corona measurements in this setup.

The second setup utilized a photomultiplier tube (PMT) to detect RF corona onset and its time delay. The three pure tungsten and three lanthanated tungsten needles that were sharpened in the same way were used in this setup and were spaced 3 cm apart from the plane electrode. The RF voltage applied to the gap is switched on for approximately 1 second at 1 minute intervals. The source path of the RF signal was modified, where the second amplifier was replaced with a different one. The updated source signal path is illustrated below, see Fig. 3.18.

Waveform	Amplifier 1	Amplifier 2	Load
Generator	43 dB gain	29.451 dB gain	Approx. 700 W
3.3 MHz	(29 dBm)	(58.451 dBm)	
-14 dBm			
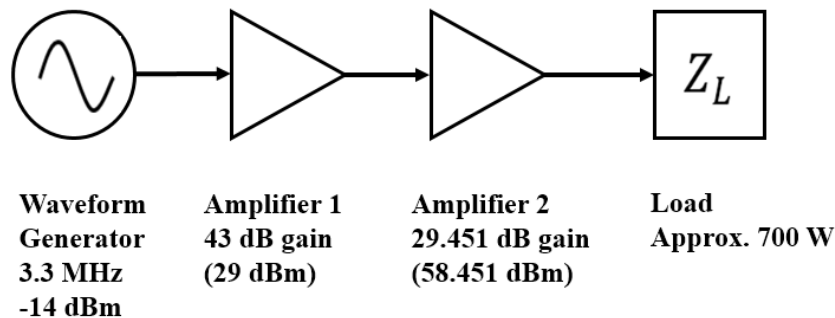
Figure 3.18. Simplified source signal path for RF corona setup using the PMT [5].

A total of 30 shots were recorded for each needle-plane configuration, totaling 180 shots for all 6 needles. Photographs of each needle's tip geometry were taken before and after RF voltage application. A simple diagram of the second setup is illustrated below, see Fig 3.19.
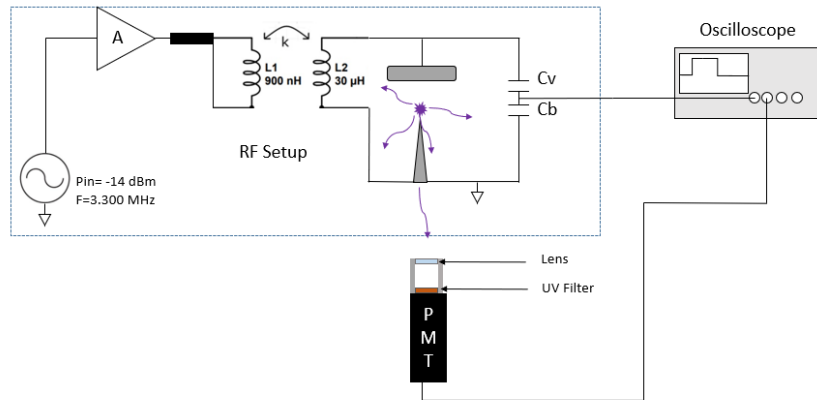
Figure 3.19. RF corona setup with implementation of PMT. The PMT signal and RF gap voltage are measured simultaneously to measure the corona onset voltage and time delay.

A PMT is a device that is capable of detecting very weak light by converting the incident photons into electrons and then amplifying them to measurable levels. Incident light passes through a quartz window and comes into contact with a photocathode. The photocathode then converts a fraction of the incident light into photoelectrons. These electrons will then become multiplied by biased electrodes called dynodes, see Fig. 3.20. At the end of the series of of dynodes, the electron avalanche reaches the anode electrode where they are collected. The electron gain of the PMT is controlled by altering the bias voltage applied to the dynodes.
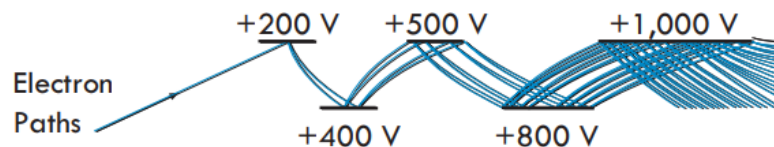
Figure 3.20. Electron path in PMT [15].

The PMT is placed 24 inches away from the center line of the needle-plane gap. The PMT gain voltage is set at 0.7 V (which translates to an electron gain of approximately $3.5x10^5$) for the entire duration of the RF corona experiment. A plano-convex

fused silica lens with a focal length of 50 mm and a UV11 color filter were fixed onto the PMT to direct the UV photons emitted from the electrode gap towards the detector and attenuate light outside of 275-400 nm. The RF voltage and PMT signal are both monitored with an oscilloscope to determine the corona onset voltage and the time delay. The time delay is measured by taking the difference between the time that the RF signal is applied and the when the PMT detects initial photons produced by RF corona in the gap. An example of how the time delay and corona onset voltage for each corona shot is shown in Fig. 3.21.
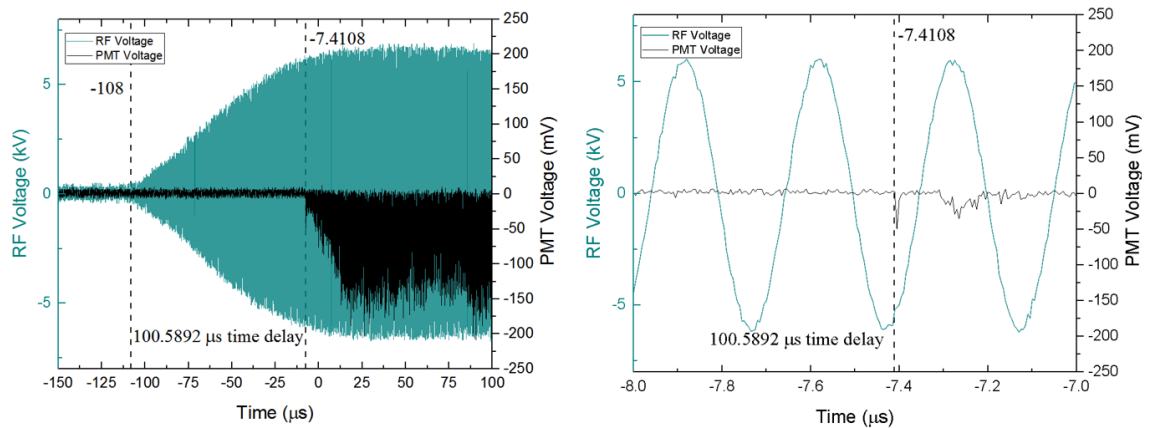
Figure 3.21. RF voltage vs PMT voltage zoomed out (left) and zoomed in at corona onset (right). The time delay for this measurement is approximately 100.5 μs. [5].

The left graph shows a zoomed out scale of the RF and PMT signals. Two vertical lines markers, one indicating the time when the RF signal starts and the other indicating when the PMT detects initial UV photons, are placed onto the graph. The difference between the two times shown for the vertical line markers is the time delay for the RF corona onset. Zooming into the section where the corona onset occurs, one can see that the first PMT signal spike occurs during the negative half cycle of the RF voltage. The magnitude of the maximum amplitude of the half cycle that the first PMT spike falls on is the RF corona onset voltage. For this particular measurement, the corona onset voltage is approximately 6.1 kV.

The oscilloscope was set to trigger on the PMT signal at -50 mV. Through trial

and error, -50 mV was selected because it was low enough to not detect noise spikes coming from the PMT while still being able to reliably capture the initial corona photonic activity measured by the PMT. The first signal spike and the noise floor of the PMT signal were differentiated by their amplitude and pulse width. The first real PMT pulse would have an amplitude of no lower than -5 mV and a slightly larger pulse width than the pulses seen on at the noise floor of the PMT signal. There were only a few measurements where it was difficult to distinguish the first real PMT signal spike from the noise floor. The time scale on the oscilloscope used was set to 1 ms/div (12 ms window) and collected over 2 Mpts per signal trace over the entire window.

3.4.3 RF Breakdown in Needle-Plane Gap Setup

RF breakdown at 3.3 MHz in a needle-plane gap was briefly investigated. Needle P3 was used and spaced at 3 cm from the plane electrode. The fast-rise RF excitation method was fed through the source path described earlier (see Fig. 3.18). A total of 20 shots were measured for this experiment.

CHAPTER 4

EXPERIMENTAL RESULTS

4.1   DC Breakdown

The DC breakdown data yielded the expected decrease in breakdown field with increasing gap distance and fall within the pd range specified for Townsend driven breakdown (c.f section 2.4), see Fig. 4.1. The measured data is compared with Eq. 2.20 and AC breakdown measurements made by Gossel [16] and Ritz [17].
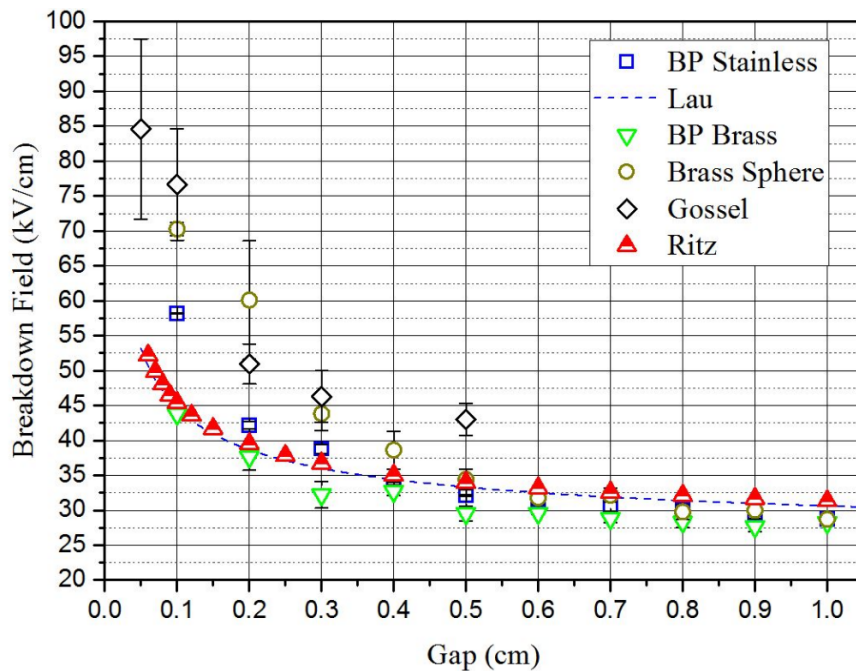
Figure 4.1. DC breakdown measurements for stainless and brass Bruce profile electrodes and spherical brass electrodes. Six measurements are made at 1 mm increments for 1-10 mm gaps. Measurements are compared with Lau, Eq. 2.20 [9] and AC breakdown measurements made by Gossel [16] and Ritz [17]. Ritz uses nickel-plated Rogowski profile electrodes of unknown diameter and Gossel takes 10 measurements per gap distance using 1 cm diameter stainless steel spherical electrodes. The error bars are calculated using the standard deviation of the data [4].

The breakdown fields measured for smaller diameter electrodes were substantially higher than larger electrodes and yielded higher standard deviations. The largest

standard deviations were observed for the smaller gaps. This behaviour is believed to be a result of the smaller electrode size and shape playing a role in the feedback mechanism for breakdown [49]. It is less likely for a photon emitted from an excited gas molecule to reach the cathode and induce photoemission on its surface if the cathode is small.

The breakdown fields measured for the stainless steel and brass Bruce profile electrodes agreed reasonably well with the breakdown curve generated by Eq. 2.20 and the measured data from Ritz. The Bruce profile data follows closely to breakdown curve down to 2 mm. Differences in the breakdown field values may be due to material properties such as impurities intermixed within the material or its tendency to form an oxide layer, which effects the feedback mechanism and the resulting breakdown field. The tendency of stainless steel to yield higher breakdown fields than other materials is noted elsewhere [43]. At 1 cm, the breakdown field measured for the brass spherical electrodes and Bruce profile electrodes was 28.3 kV/cm, which is close to the often cited 30 kV/cm breakdown field for atmospheric air.

Using Eq. 2.17 and the DC breakdown data for the Bruce profile electrodes, the second Townsend ionization coefficient γ, is calculated, cf. Fig. 4.2.
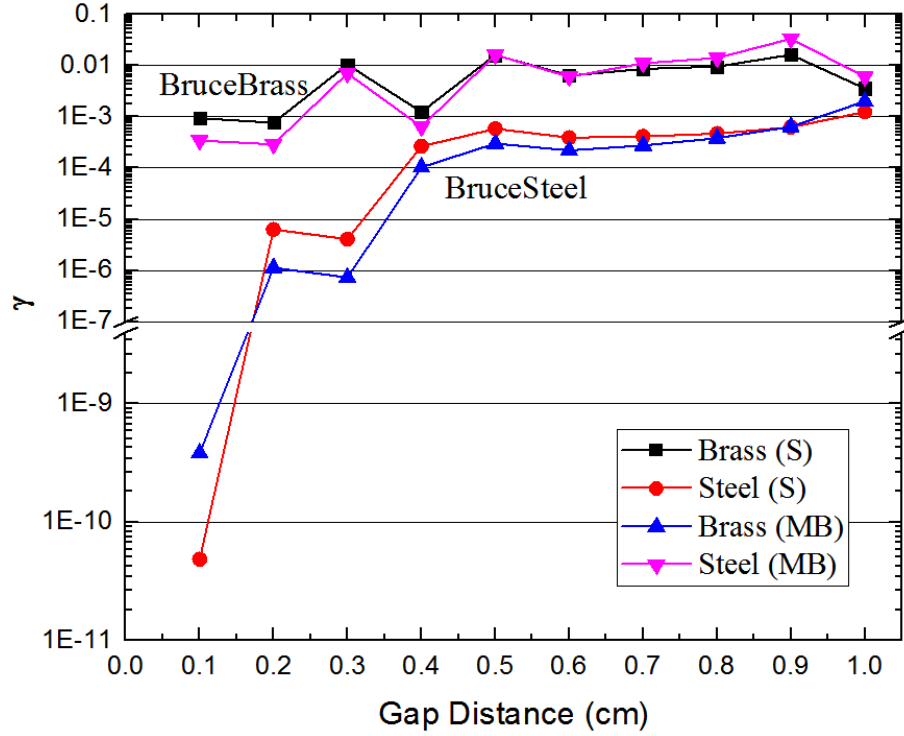
Figure 4.2. Calculated γ using DC breakdown voltage data for stainless steel and brass Bruce profile electrodes [4]. γ is calculated using α_e from Multibolt (MB) [7] and the equations from Sarma (S) [8].

The effective ionization coefficient α_e was calculated using Multibolt (MB) [7] and the equations from Sarma (S) [8]. There was fairly good agreement between γ (MB) and γ (S) for the stainless steel and brass electrode configurations. The calculated γ (MB) and γ (S) at 1 mm for the stainless steel electrode configuration were approximately 1 order of magnitude apart from each other. After performing an extensive literature survey on α for air, it was found that there are many inconsistencies in the reported values. Small changes in the value for alpha can result in a large impact when calculating γ due to the exponential dependence in Eq. 2.17. Therefore, the values for γ presented in Fig. 4.2 should be taken with some caution. The values calculated using the breakdown data of the brass Bruce profile electrodes were nearly within the 0.001 to 0.01 range reported by Nasser [1]. On the contrary, the values for the stainless steel Bruce profile electrodes are lower and decrease drastically at gap

distances lower than 3 mm. This would suggest that breakdown of gaps lower than 3 mm using stainless steel electrodes no longer purely follows the Townsend mechanism and that surface effects effects take over. Gossel [16] also reported higher breakdown fields in small gaps using stainless steel electrodes (see Fig. 4.1), further supporting that the breakdown fields using stainless steel occurs at comparatively higher fields.

DC breakdown measurements using different Bruce profile electrode material configurations revealed that the breakdown amplitudes were affected primarily by the choice of cathode material. see Table 4.1.

Table 4.1. DC breakdown field measurements for different electrode material configurations at 5 mm gap distances. Ten consecutive shots are measured per electrode configuration. AK indicates the electrode placement in the circuit where A is the anode and K is the cathode. SS-DC: stainless steel anode and cathode, SB-DC: stainless steel anode and brass cathode, BS-DC: brass anode and stainless steel cathode, BB-DC: brass anode and cathode. [4].

Electrode Configuration and Excitation Method	Breakdown Field [kV/cm]	Standard Error
SS-DC	30.83561	0.12276
SB-DC	29.82285	0.54282
BS-DC	31.05999	0.10331
BB-DC	30.15019	0.24324

Configurations with a brass cathode exhibited lower breakdown field amplitudes with a larger standard deviation than its stainless steel counterpart. The overall effect of the cathode is expected since γ will vary with different electrode materials. The effect that was measured is statistically significant and can be easily reproduced.

4.2   RF Breakdown

Having established a baseline by comparing the DC breakdown results with literature, the DC results are then compared with RF measurements made with Bruce profile electrodes at a 5 mm gap, see Table 4.2.

Table 4.2. Breakdown fields at 5 mm gaps of various Bruce profile electrode configurations and excitation methods compared to the excitation method with the fastest rise time in the set. AK describes the electrode arrangement in the configuration where A is the anode and K is the cathode. S: stainless steel; B: brass; slow: slow-rise time RF signal with approx. 5 mV/μs; fast: fast-rise time RF signal with 200 V/μs rise; DC: DC field; faster; faster-rise RF signal with approx. 414 V/μs rise [4].

Electrode Configuration and Excitation Method	Breakdown Field [kV/cm]	Standard Error
SS-Slow	25.5926	0.28429
BS-Slow	26.144	0.24646
SB-Slow	26.3018	0.34488
BB-Slow	26.136	0.48275
SS-Fast	29.1764	0.16936
BS-Fast	27.778	0.43548
SB-Fast	28.648	0.47611
BB-Fast	28.316	0.49286
SS-DC	30.83561	0.12276
SB-DC	29.82285	0.54282
BS-DC	31.05999	0.10331
BB-DC	30.15019	0.24324
SS-Faster	37.31429	2.29605

The slow-rise measurements on the left side of the graph yielded results similar to literature on the topic [1] and simulations at 3.3 MHz [10]. Comparing to the DC measurements, the slow-rise RF measurements yielded 83% of the DC breakdown field amplitude. Slowly increasing the RF voltage in the gap provided sufficient time for electrons to enter the gap and for the ion space charge to accumulate [1].

RF breakdown produced by fast-rise excitation yielded approximately 90% of the DC breakdown fields. The even faster excitation method produced RF breakdown fields greater than 120% of the DC breakdown fields. The standard deviation for the faster-rise data point is 640 V, which is substantially larger than its 54 V DC counterpart. This behavior is expected to be a consequence of the application of a fast rising RF field in the gap. It has been shown that the breakdown field, given a

set gap distance and pressure, is a monotonically falling function of the breakdown time lag in unipolar fields, cf. Fig. 14 in ref [50] and in microwave fields, cf. Fig. 5 in ref [51]. The time delay of the breakdown is on the same order as the rise time of the applied RF signal (meaning that the RF breakdown occurs on/near the rising edge of the RF signal). Therefore, the RF breakdown voltage is also a monotonically falling function of the rise time. The result of this is the breakdown voltage rises when the rise time is reduced.

There was interest in seeing if seeding electrons in the gap could reduce the standard deviation observed for the faster-rise RF breakdown measurement (see Fig. 4.2). Thus, UV light was applied to the gap to induce photoemission on the electrode surfaces. The results of the UV applied faster-rise breakdown is compared with other excitation methods with the same electrode configuration, see Table 4.3.

Table 4.3. Comparison of UV-seeded RF breakdown in faster-rise fields against different excitation methods without application of UV. Identical electrodes are used for all cases at 5 mm gaps. Slow: slow-rise time RF signal with approx. 5 mV/μs; fast: fast-rise time RF signal with 200 V/μs rise; DC: DC field; faster; faster-rise RF signal with approx. 414 V/μs rise [4].

Electrode Configuration and Excitation Method	Breakdown Field [kV/cm]	Standard Error
SS-Slow	25.5926	0.28429
SS-Fast	29.1764	0.16936
SS-DC	30.83561	0.12276
SS-Faster	34.7586	1.28505
SS-Faster-UV	32.6294	0.2242

The faster-rise RF breakdown field yielded a substantially lower standard deviation and magnitude than without UV, see the right 2 data points in Fig. 4.3. The statistical time delay of the breakdown was largely eliminated by the presence of photoelectrons in the gap when the RF pulse was applied. The gap breaks down earlier on the rising edge of the applied RF signal, but remains at a higher breakdown am-

plitude than the slower rise time counterparts. Taking in consideration the difference of the UV applied and non UV faster-rise breakdown measurements, the formative time lag of the breakdown can be estimated to approximately 40 μs.

Measurements of faster-rise RF breakdown spanning 1-5 mm (rise times > 1000 μs) with and without UV application are graphed below, see Fig. 4.3.
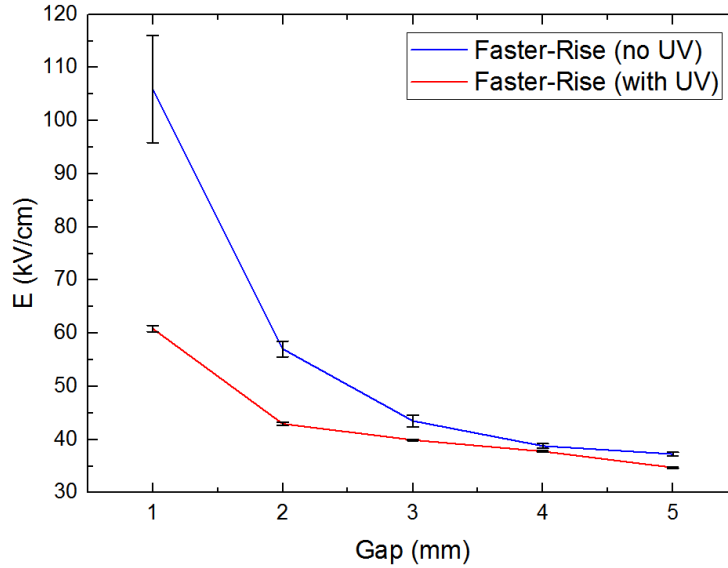
Figure 4.3. Measured RF breakdown field ranging from 1-5 mm gaps with and without UV application. Six measurements are recorded for each gap distance.

The non UV data yielded the highest amplitude (105 kV/cm) and standard deviation at 1 mm. The large amplitude and standard deviation observed at 1 mm is a consequence of the small gap and the role of the statistical time lag. Using the estimates made by Chrisophorou [52], the number of electrons that are generated by ionization via cosmic radiation and terrestrial sources for atmospheric air is ~ 12 $\frac{1}{cm^3 \cdot s}$. The probability of an electron being present in the gap to initiate breakdown is much lower in small gaps than in larger gaps. As one would expect, the statistical time lag increases, allowing the field to rise to higher amplitudes under the very fast rise excitation. As the appearance of an electron in the gap is a statistical process, the standard deviation of the breakdown field will also be fairly large. As the gap size increases, the statistics on the measured breakdown field decrease significantly. A

larger gap means there is more of a chance of an electron being in the gap to initiate breakdown. With UV application in the gap, the statistics are brought down to a minimum as a result of seeding electrons in the gap.

Faster-rise RF breakdown with UV applied to gap was imaged with an ICCD camera to observe the development of prebreakdown, see Fig. 4.4-4.7.
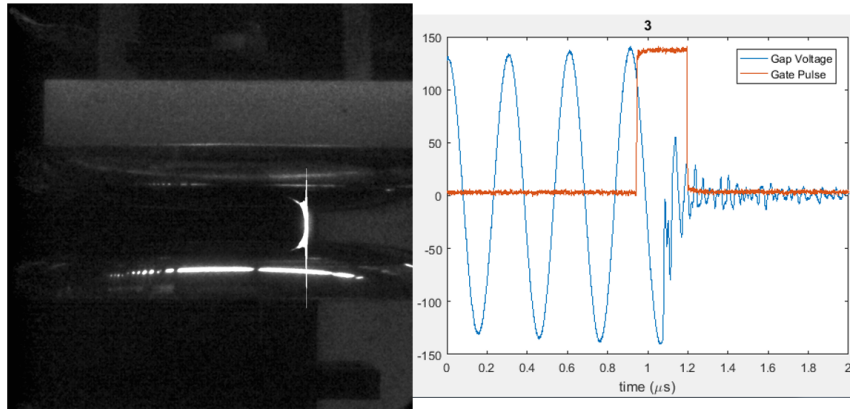
Figure 4.4. Example of saturated ICCD image of electrode gap due to RF breakdown (left) and corresponding RF voltage overlaid with the scope trigger signal (right).

Acquiring the correct timing for between the ICCD gate pulse and the time before the RF breakdown event took much trial and error. Often times, the gate pulse would overlap with the breakdown event, resulting in the ICCD capturing a bright arc and saturation, see Fig. 4.4. Note that the breakdown event occurs when the sinusoidal signal collapses entirely. Other times, the ICCD gate pulse would happen several cycles before the breakdown event, which would result in the camera missing the prebreakdown development and breakdown event entirely, see Fig. 4.5. The reason for the high degree of breakdown/missed shots is due to the statistical nature of breakdown. While the UV applied to the gap reduces the breakdown amplitude fluctuations significantly, the little variation that remains is large enough to make the time delay of the breakdown inconsistent. The delay of the gate pulse would need to be set to where the gate pulse occurs during a time scale where breakdown could occur. Then, multiple shots would need to be taken until the gate pulse falls right

before the RF voltage collapses.
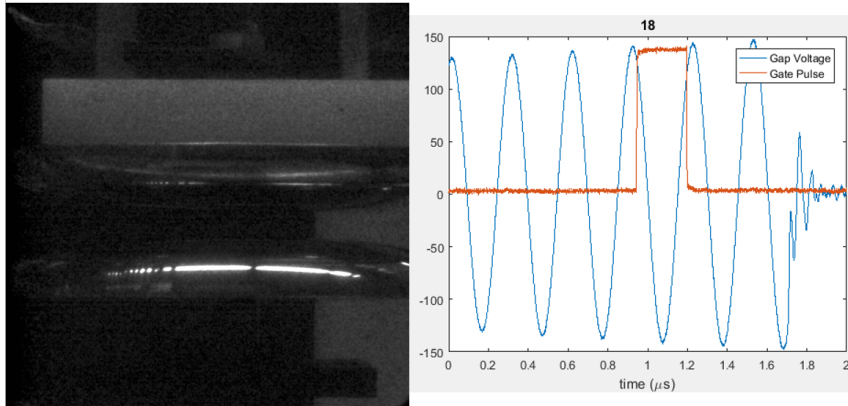
Figure 4.5. Example of a missed shot ICCD image of electrode gap (left) and corresponding RF voltage overlaid with the ICCD gate pulse (right). Note that the pulse from the scope rises and falls 1 and a half cycles before breakdown occurs.

Of the 18 shots that were measured and imaged, only 2 of them were reasonably close to the timing desired to capture prebreakdown, see Fig. 4.6 and 4.7. The first well timed shot occurred on the first shot of the set. The gate pulse ends right at the beginning of the breakdown event, resulting in the ICCD capturing an image of a single breakdown channel in the gap. The ends of the channel are slanted at angle, which is due t the light from the channel being reflected off the electrode surface. The last shot in the set also yielded favorable timing conditions and a similar captured image as seen for the first shot. This time, a more faint single channel formed towards the center of the gap.
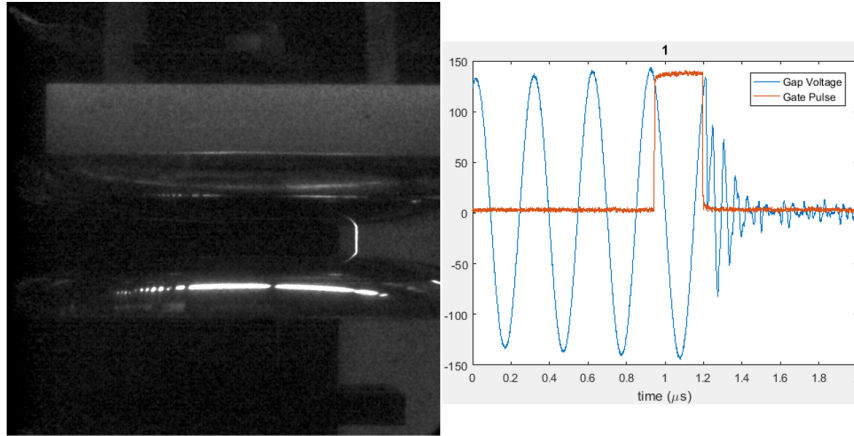
Figure 4.6. ICCD camera image of single channel RF breakdown (left) and corresponding RF voltage overlaid with ICCD gate pulse (right). The gate pulse rises and falls just before the breakdown occurs.
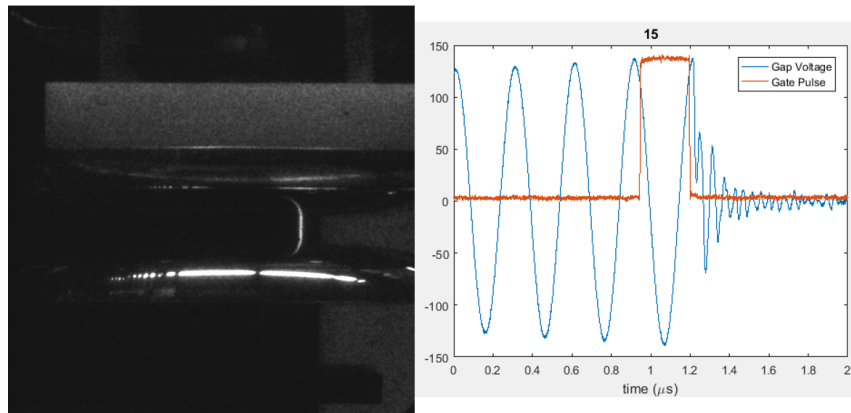
Figure 4.7. ICCD camera image of single channel RF breakdown (left) and corresponding RF voltage overlaid with ICCD gate pulse (right). The rise and fall of the gate pulse occurs right before the breakdown event.

Overall, acquiring the optimal timing with the RF voltage and ICCD gate pulse proved to be a difficult task due to the variability in the RF breakdown amplitude. The imaging revealed that RF breakdown tends to favor a single channel. By irradiating the electrodes with UV, electrons will be liberated from the metal surface. These electrons will then get accelerated in the gap and ionize the surrounding gas. It is postulated that once ionization begins in a certain spot, the current will favor that spot and amplify until breakdown occurs.

4.3   DC Corona

In the needle-plane configuration using the machined tungsten needle, I-V and V/I curves were generated for both positive and negative needle corona, cf. Fig 4.8.
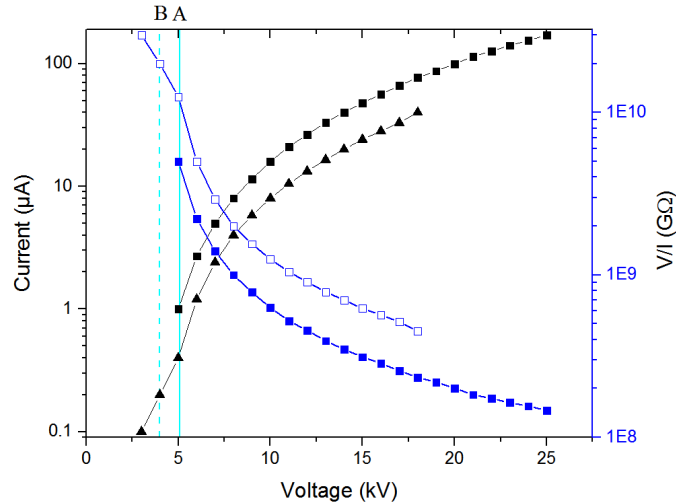
Figure 4.8. I-V and V/I curves for positive and negative needle corona using the machined tungsten needle with a 2 cm gap. V/I is calculated and plotted to compare to the current draw. Reference line A: RF corona onset voltage; Reference line B: RF corona extinguished voltage [4].

For the negative needle, the minimum corona current (approx. 1 μA) was detected at 5 kV and a visible glow was observed at 8 kV. As voltage is increased, the current increases at a positive nonlinear trend. At its peak, the current measured was approximately 200 μA.

The I-V curve for positive needle corona assumes a similar shape as the I-V curve for the negative needle. At the same 1 μA current, the voltage measured is 1 kV higher what was measured in the negative needle corona configuration. Visible glow was not observed until 15 kV, which is 7 kV higher than negative needle corona. However, the current draw for the positive needle corona with respect to voltage is lower than what was measured for negative needle corona. The negative draws more current because it easily emits electrons due to the enhanced field at the tip. The positive needle corona will not draw as much current because the negative plane electrode is not a good source of electrons due to its flat surface. Therefore, the electrons have

to come from the surrounding air, which are inherently fewer in number than what is produced by field emission on the negative needle corona. The V/I curves reflect this, showing that the maximum for the positive needle is over 6 times larger than the negative needle.

IV curves for positive and negative needle corona using the pure tungsten electrodes with varying included angles (31.4° and 44.4°) were graphed as well, cf. Fig. 4.9 and Fig. 4.10 [5].
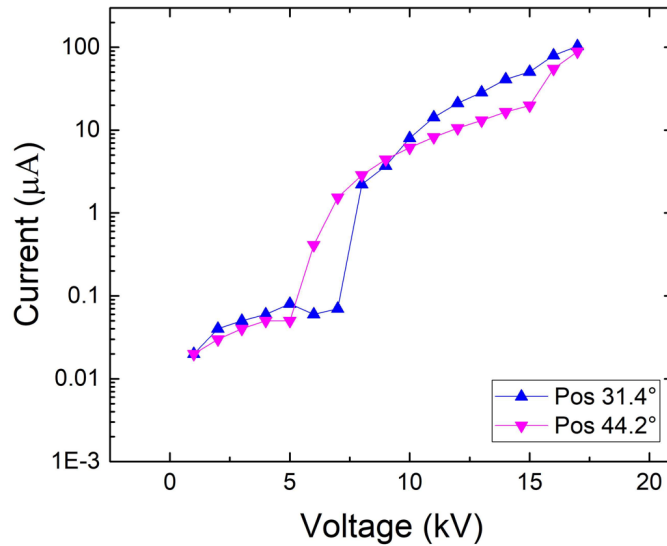
Figure 4.9. Voltage and current measurements of positive needle corona using 31.4° and 44.2° pure tungsten needle electrodes [5].

Starting at 1 kV, the measured current for the positive and negative needles increases gradually with increasing voltage up until a certain point (marked by the sharp rise in current). If smaller currents had been measured in the machined tungsten needle configuration, the IV curves for the positive and negative needles in Fig. 4.8 would look similar to the positive and negative IV curves shown in Fig. 4.9 and Fig. 4.10.

The measurements revealed that the 31.4° needle electrode ignited positive and negative corona at lower voltages than the 44.2° needle electrode as expected. For simplicity, the corona onset will be marked by the DC voltage before the first sharp

current spike. With a smaller included angle, the effective emitter area is reduced, creating a larger field enhancement than the needle electrode with the larger included angle. A large field enhancement will amplify electron multiplication and ionization processes, leading to a lower corona inception voltage. The negative needles yielded lower inception voltages than the positive needles, confirming what has been reported in literature [1, 2]. The 44.2° needle yielded an onset voltage of 6 kV when negative and 7 kV when positive. Similarly, the 33.4° needle yielded an onset voltage of 4 kV when negative and 5 kV when positive. A 1 kV difference between the onset voltage for positive and negative needles is noted.

As the voltage is increased, the current increases gradually up until a critical voltage is reached in which the current begins to rise at an increased rate. At this point, the gap becomes significantly more conductive and draws more current, igniting corona. Beyond this point, the rate at which the current rises gradually declines with increasing voltage. This gradual rise in current after the sharp rise is evident in both the positive and negative needle IV curves.
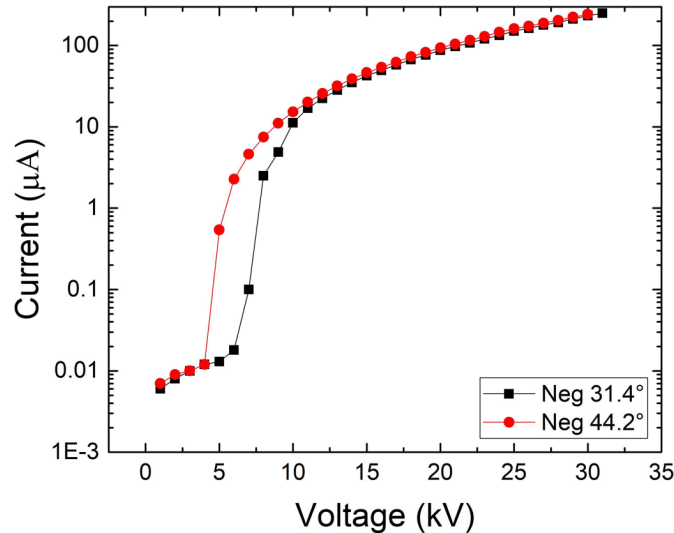
Figure 4.10. Voltage and current measurements of negative needle corona using 31.4° and 44.2° pure tungsten needle electrodes [5].

Starting at 15 kV, the current for positive corona undergoes a second sharp rise before ultimately breaking down at 18 kV, which agrees well with a measured 17.55

kV breakdown voltage in a 2 cm needle-plane configuration reported elsewhere [53]. The graphed current for the negative needle (see Fig. 4.10) does not undergo a second current spike like the positive needle due to reaching the limits of the high potential source (approx. 30 kV). The result of positive needle configurations having a lower breakdown voltage than negative needle configurations is reported in literature [12]. In the case of positive needle corona under steady state conditions, the electrons move towards the positive needle, leaving behind a positive space charge. This positive space will drift towards the negative plane electrode. While the positive space charge effects decreases the enhanced field of the positive needle, it will also increase the ionization region as it moves away from the needle. The field created between the positive space charge and the negative plane electrode may become large enough to initiate a cathode directed streamer, which can ultimately lead to breakdown of the gap. In the negative needle case, electrons are deflected towards the lower field region in the gap, which leaves a positive space charge behind that drifts towards the negative needle. While the positive space charge greatly enhances the field at the tip of the negative needle, the depth of the ionization region is greatly diminished. When ionization ends, the positive and negative charges are swept out of the gap by the macrofield and the cycle is repeated. To overcome this cycle, a higher bias voltage must be applied to the needle-plane gap, hence the higher breakdown voltage threshold for the negative needle versus the positive needle. Based on experimental data reported in literature [53], the expected breakdown voltage of the negative needle with a 2 cm gap is approximately 40 kV.

4.4   RF Corona

The peak RF power with respect to RF voltage using the machined tungsten needle electrode in a 2 cm gap is shown below, see Fig. 4.11.
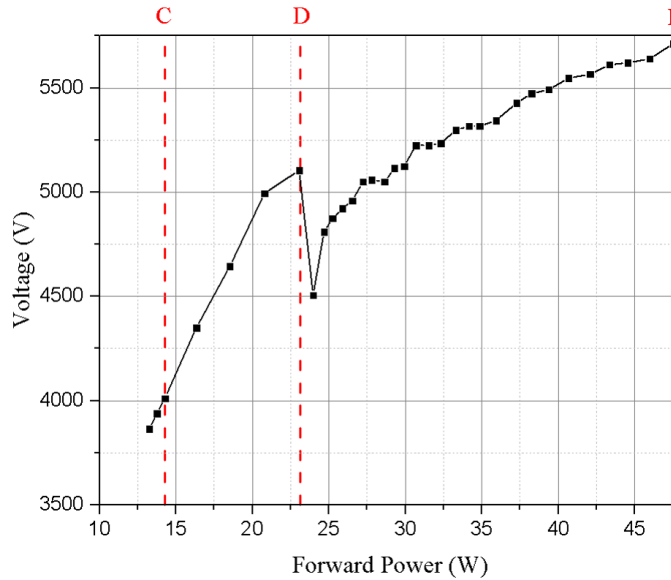
Figure 4.11. RF corona voltage measurements with respect to applied rms power using machined tungsten needle with in a 2 cm gap. The power is stepped up by 0.1 dBm increments after reference line D. Reference line D - corona onset power; reference line E - RF breakdown power; reference line C - RF corona extinguished power [4].

From 13 W rms to 21 W rms, the RF voltage increases almost linearly with applied forward power. At the point just before visual onset of RF corona was observed (reference line D), there is a noticeable change in slope. One may argue that weak corona is forming at 21 W rms already. After reference line D, the voltage drops from 5.1 kV to 4.5 kV, showing that the LC circuit is being loaded down by the corona. The RF corona onset voltage seems to be the same as DC the onset value marked by reference line A, cf. Fig. 4.8. However, it is roughly estimated that the RF corona draws roughly 1 order of magnitude higher current than DC corona. The 1-2% drop from the linearly interpolated voltage before visual onset of corona (reference line D, cf. Fig. 4.11) can be reproduced by introducing RF current flowing in parallel with C_{eff} of the simplified RF circuit model, see Fig. 3.10 [4]. In addition, the larger current draw in RF corona can be explained by the accumulation of positive and negative charges in the gap as a consequence of the high frequency field being applied.

After reference line D, the input power is stepped up by 0.1 dBm increments until breakdown occurs (after reference line E). Similar to the onset of RF corona, the voltage drops again due to the sharp rise in current being drawn from the plasma arc from breakdown [4]. At a 2 cm gap, the onset of RF corona at 5.1 kV will remain ignited down to 4 kV. Below 4 kV, the RF corona extinguishes on the needle. Based on these conditions, RF corona in a 2 cm gap needs approximately 23 W rms to ignite in the LC circuit. The macroscopic field in this configuration is 2.55 kV/cm, which translates to roughly 85 kV/cm on the tip, yielding a field enhancement factor of β ~ 33.3, acquired from electrostatic simulations [4].

The results gathered from the RF corona measurements showed that extra care must be taken when fabricating the ESA [20] since any sharp corners or protrusions must be minimized. To avoid corona formation in the ESA with a macrofield of 20 kV/cm at 500 kW, a protrusion with a radius of 0.05 mm must be no taller than 0.07 mm [4]. This indicates that the smoothness of the surfaces within the ESA geometry should be considered. Overall, it is recommended that any structures within the ESA should be smooth, tapered, and have a large radius to reduce field enhancements and avoid corona losses.

Experimental measurements were carried out for RF corona onset voltage and time delay for using the set of pure tungsten and lanthanated tungsten needles sharpened in the same way. The envelopes of the RF and PMT signals are graphed below, see Fig. 4.12.
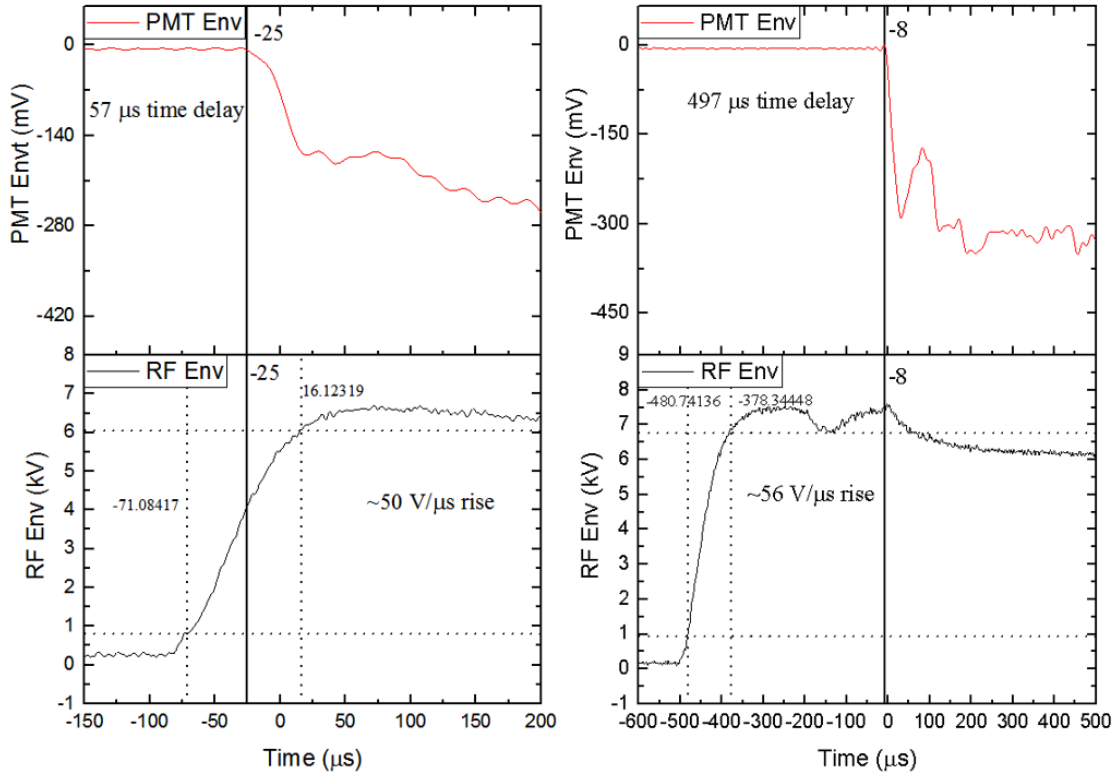
Figure 4.12. Envelopes of RF and PMT signal of the 1st shot of needle P5 (left) and the 30th shot for needle L4 (right). The rise time of the RF envelope is determined by taking the difference of the 10% and 90% point of the rising edge. The rise times for these particular shots are 50 V/μs and 56 V/μs, respectively [5].

Vertical line markers indicating the corona onset are placed on both the RF and PMT envelope graphs. The placement of these markers are confirmed by examining the raw RF and PMT signal like shown earlier in Fig. 3.21. Additional horizontal and vertical line markers are placed on the RF envelope graphs to determine the rise time of the RF signal. The markers are placed at the 10% and 90% marks of the RF envelope rising edge. Examining the RF and PMT measurements revealed that earlier onset of corona slightly decreases the rise time of the RF signal. The rise time of the RF voltage is determined by the Q of the RF circuit [30]. When the corona onset occurs on the rising edge, the RF circuit starts to get loaded down, which in turn decreases the Q and decreases the rise time. In the case when the RF onset occurs well past the rising edge of the applied RF voltage (see right graph of Fig. 4.12

the rise time is typically 56 V/μs.

The total corona onset voltage and time delay data points for the 3 pure tungsten and 3 lanthanated tungsten needles are graphed in Fig. 4.13.
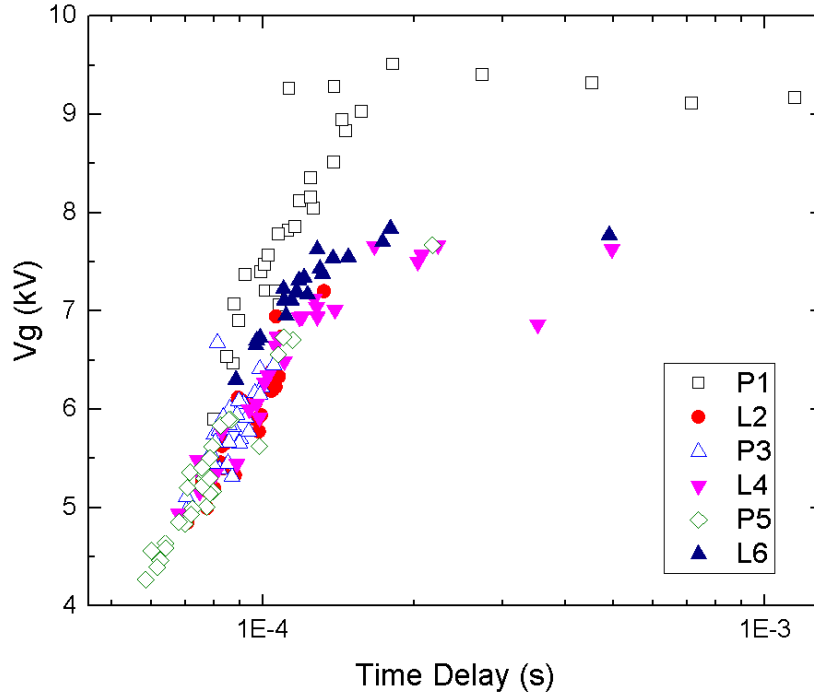
Figure 4.13. Corona inception voltage and time delays for pure tungsen and lanthanated tungsten needles. 171 data points (90 pure tungsten and 81 lanthanated tungsten needles measurements) are graphed. P - pure tungsten; L - lanthanated tungsten. The needles (see legend) are numbered by the order in which they were measured. Note: 21 data points are graphed for (L6) [5].

The time delays measured for the needles spanned between 58 μs to 1.14 ms. Most of the time delays occurred at times less than 200 μs. Needles L4 and L6 showed similar time delays and corona onset voltages (68-500 μs and 4.8-7.6 kV) while the range of needle L2 stops at 130 μs and 7.2 kV. Needle L2 is believed to have a smaller needle geometry compared to the other lanthanated needles since it exhibited a smaller range for the corona onset and time delay than needles L4 and L6. To confirm this, the needle tip photos of needles L2, L4, and L6 are compared below, see Fig. 4.14.
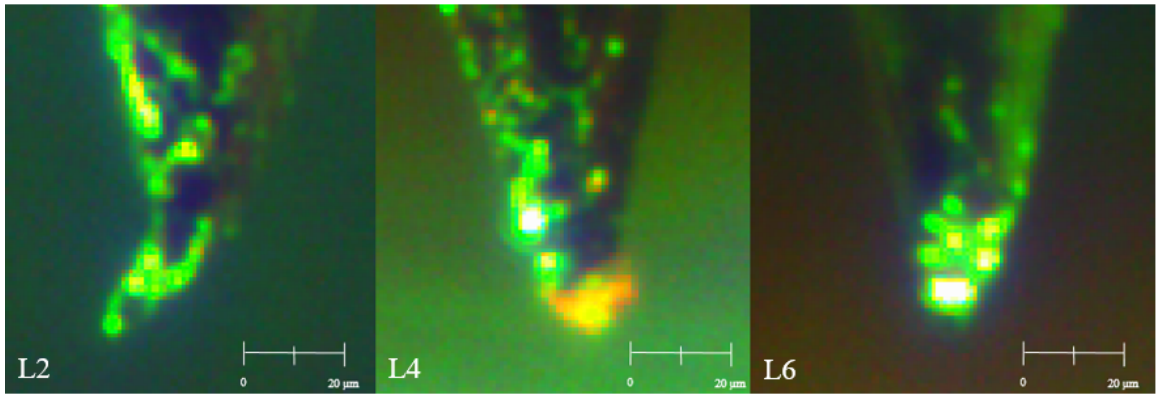
Figure 4.14. Lanthanated tungsten (L) needle tip photos before application of RF voltage. L2 (left); L4 (middle); L6 (right) are compared [5].

As predicted, needle L2 has a noticeably smaller tip geometry than needles L4 and L6. The smaller tip geometry of L2 will behave as a larger field enhancement when the RF voltage is applied and field emit electrons in less time than needles L4 and L6. Therefore, the time delays for needle L2 will occur at shorter times than needles L4 and L6. L4 and L6 have very similar tip geometries, so it is unsurprising that their corona onset voltages and time delays fall within the same range.

Amongst the pure tungsten needle data points, there was a group that exhibited considerably higher onset voltages and longer time delays, see Fig. 4.13. These group of data points belong to needle P1 in the experimental data set. The higher onset voltages measured for needle P1 are believed to be due to its larger tip geometry. Like carried out for the lanthanated needles, the images of the tip geometries of the pure tungsten needles are compared, see Fig. 4.15.
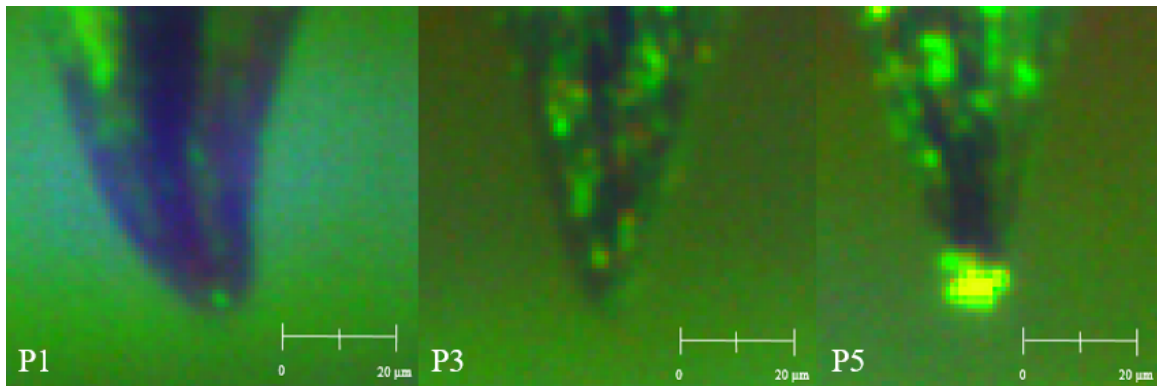
Figure 4.15. Pure tungsten (P) needle tip photos before application of RF voltage. P1 (left); P3 (middle); P5 (right) are compared [5].

It is evident that the needle tip geometry of needle P1 is larger than needles P3 and P5. Since the corona onset voltage is proportional to emitter radius, accordingly needle P1 would require a higher RF voltage to ignite corona than the other tungsten needles with smaller emitter radii.

It was observed in pure tungsten needles that the corona onset showed preference in igniting when the needle is in negative polarity. The positive and negative half cycle in which the needle electrode ignites is termed positive needle and negative needle ignition. It is noted that the RF voltage is inverted to correctly reflect the positive half cycle as positive needle and the negative half cycle as negative needle. Fig. 4.16 shows examples of positive and negative needle ignition.
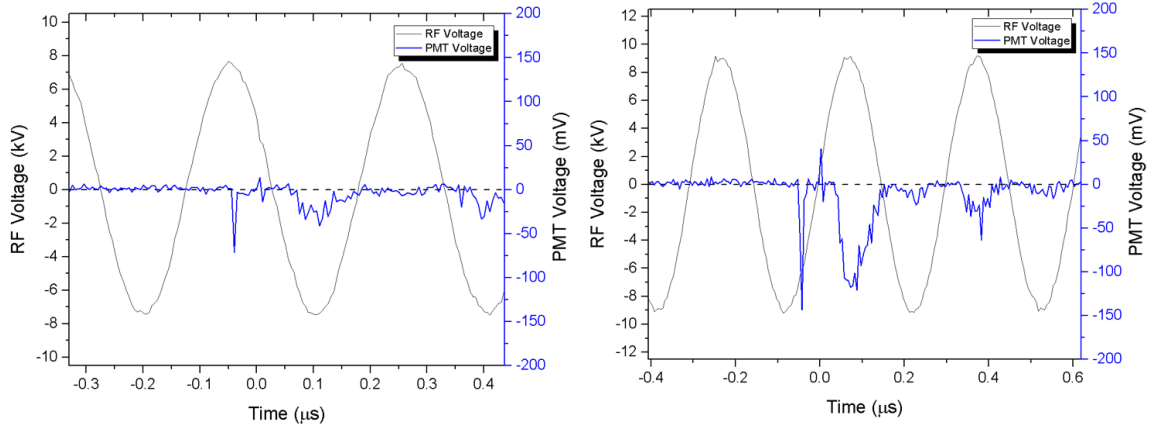
Figure 4.16. Positive needle ignition (left) and negative needle ignition (right) waveforms [5].

RF corona forming on the lanthanated needles show no preference with essentially an equal number of shots igniting on the positive (48.14%) and negative (51.85%) polarities. Pure tungsten needles showed preference on igniting during the negative polarity (27.77% positive and 72.22% negative). The total number of ignitions for the needles used in the RF corona experiment are tabulated in Table 4.4.

Table 4.4. Total positive and negative needle ignitions for the pure tungsten and lanthanated tungsten needles [5].

Needle	Positive Ignitions	Negative Ignitions
P1	4	26
L2	15	15
P3	4	26
L4	14	16
P5	17	13
L6	10	11

Unlike needles P1 and P3, needle P5 showed a tendency to ignite during the positive polarity. Removing the sharpest (L2) and bluntest (P1) needles from the data set, the behavior of the RF corona ignitions on the lanthanated needle barely changes (47.06% positive and 52.94% negative) while the pure tungsten needle behavior is affected more, but still showing preference on igniting on the negative polarity (35%

positive and 65% negative). This behavior may be due to microprotrusions on the tip of the pure tungsten needle. If the microprotrusions are small enough and the field is sufficiently high, they will field emit electrons during the negative polarity. The field emitted electrons would then excite nearby molecules, to which they may yield UV photons via spontaneous emission and ultimately get detected by the PMT within the time frame of the negative polarity. On the contrary, the surface conditions of the lanthanated needles and P5 may not be viable for field emission to occur given the magnitude of the applied RF field. Hence, the initiatory electron would come from the volume and show no preference in corona igniting on the positive or negative polarity. Further analysis of the tip surface conditions via scanning electron microscopy would be necessary to validate this theory.

It was discussed earlier that there was a group of data points with noticeably larger corona onset voltages and longer time delays as a consequence of a larger emitter radius for needle P1, cf. Fig. 4.13. In light of this, the total data for Fig. 4.13 is plotted without the inclusion of P1 to analyze the data for needles that are grouped more closely together, see Fig. 4.17.
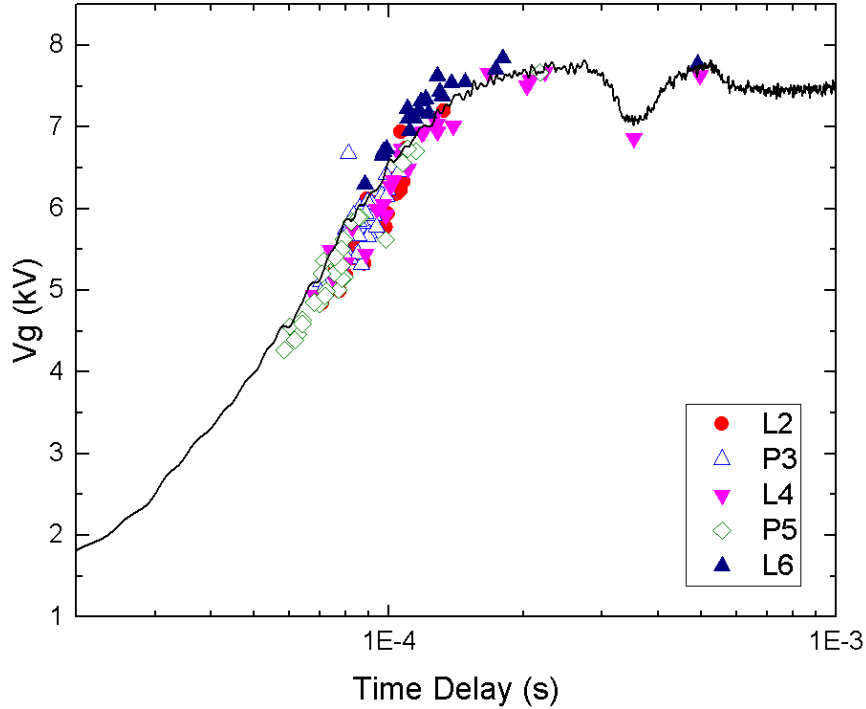
Figure 4.17. RF corona onset voltage and time delay plotted omitting data points from P1. The envelope of the applied RF signal (black curve) is fitted and overlaid on the data points [5].

The data points for the remaining pure tungsten and lanthanated tungsten needles follow closely with the RF envelope, as it should. There is one outlier amongst the P3 data at 80 μs. One can see that almost all of the measurements occur on the rising edge of the RF envelope. The measured onset voltages span from 4.2 kV to 7.5 kV. In a similar experimental setup examining 5 MHz corona for a single needle geometry, Auzas reports that their RF onset voltage starts above 6 kV [30], which is in the range of the graphed onset voltages of Fig. 4.17.

In general, there appears to be no significant difference between the pure tungsten and lanthanated tungsten RF corona data, which implies that the choice of material does not affect the corona onset voltage at 3.3 MHz. In the case of AC welding, lanthanated tungsten needles are known to ignite and sustain an arc at lower voltages than pure tungsten needles. This behavior is likely not occurring here because the experimental conditions are far from the much hotter temperature regime for welding,

which supports a fully formed plasma arc rather than a comparatively weak corona. Furthermore, the frequency that is used in most AC welding applications lies between 80-200 Hz, which is several orders of magnitude lower than the 3.3 MHz frequency being applied in this experiment.

The process resulting in the diffusion and evaporation of lanthanum in welding is much larger than the current being drawn by the needle electrode in the RF experimental setup (tens to hundreds of A vs a few mA). The high current utilized in welding will heat up the electrode, causing the lanthanum to diffuse towards to the tip of the needle. The evaporation of the lanthanum oxide lowers the work function of the needle electrode, reducing the necessary voltage to keep the arc active. The current drawn in the experimental setup is too small to sufficiently heat the lanthanated tungsten needle electrode to cause diffusion of the lanthanum embedded in the bulk material. While lanthanum is present on the surface of the electrode, it is not sufficient enough to make a noticeable difference in the corona onset behavior compared to the pure tungsten needle electrode.

A 2D electrostatic simulation of the needle-plane geometry was carried out to find an estimate of the enhanced field on the needle electrode tip, see Fig. 4.18. The geometry of needle P3 was used in the electrostatic simulation since it exhibited the most symmetrical tip geometry compared to the rest of the needles. The tip geometry was approximated by fitting a circle onto the electrode. The emitter radius, which is the radius of the circle that was fitted, is approximately 8 μm. Utilizing a corona onset voltage of 5.8 kV, which was found by taking an average of all the RF corona onset voltages for P3, yielded a maximum enhanced electric field of 1.65 x 10^8 V/m along the center line of the needle tip. As a result, the field enhancement factor of the needle tip is $\beta \sim 850$.

The magnitude of the electric field found by the electrostatic simulation is not large enough to be in the range of field emission, which is said to start when the field is on the order of $\sim 10^9$ V/m [1]. To establish a point of reference, it is assumed that field emission becomes significant when the tip is emitting 1 electron per microsecond.

81

Using Eq. 2.8, the magnitude of the enhanced field must be at least 1.81 x 10^9 V/m for the tip to emit 1 electron per microsecond. For thermionic field emission (Eq. 2.9) to occur at the assumed rate described for field emission, the temperature of the of the tip must must reach 1407 K. Temperatures of that magnitude are not feasible with the mA level current being drawn by the needle. A simplified estimate of Joule heating at the needle tip over 1 second (no heat loss mechanisms considered) yielded a 20 K increase from room temperature (313 K) at best. Realistically, the calculated change in temperature would be smaller if loss mechanisms were introduced. Thus, it would be safe to assume that thermionic emission is not initiated at the tip given the experimental conditions. Likely, the initial electron to start the development of RF corona originates from the volume rather than from field emission or thermionic emission of the needle electrode tip. It is noted that the estimated number of electrons freed due to cosmic radiation and terrestrial sources in air (12 electrons $\frac{1}{cm^3 \cdot s}$) would not be sufficient as the source of initiatory electrons for the RF corona observed in the experiment. It is very unlikely that an electron freed by cosmic radiation/terrestrial sources will show up near the needle on the microsecond or millisecond time scale. A more likely source of initiatory electrons in the volume may come from field assisted electron detachment, where weakly bound electrons in ion clusters (average of ~ 1000 $\frac{ions}{cm^3}$ in altitude of 0 to 18 km [54]) are detached in the presence of a strong electric field [55].
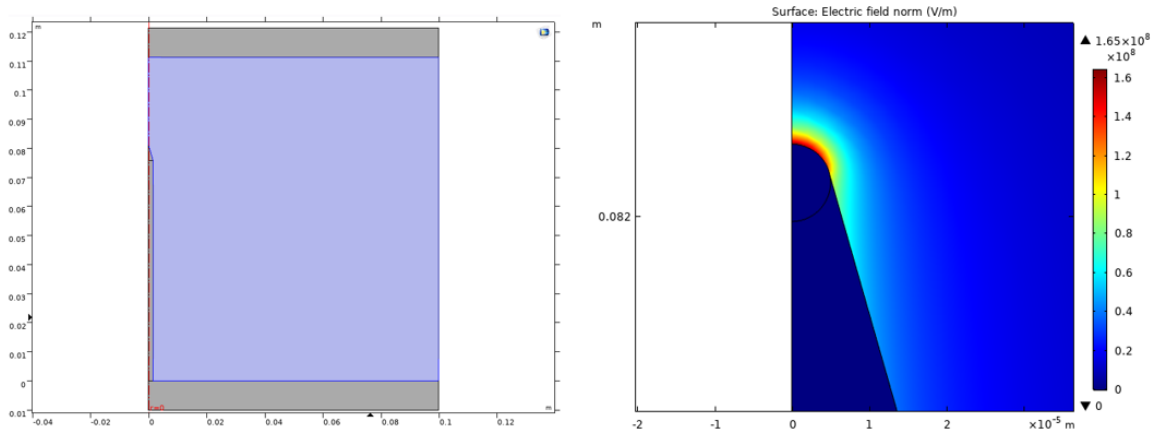
Figure 4.18. 2D electrostatic simulation of needle P3 in COMSOL. The needle is symmetrical about the Z-axis. Maximum electric field along the center line is 1.65 x 10^8 V/m [5].

The RF and PMT voltage after some time after the corona onset initiated is shown in Fig. 4.19. Large voltage spikes are observed in the PMT signal when the needle is positive while smaller voltage spikes are observed when the needle is negative. This behavior is consistent for both pure tungsten and lanthanated tungsten needles.
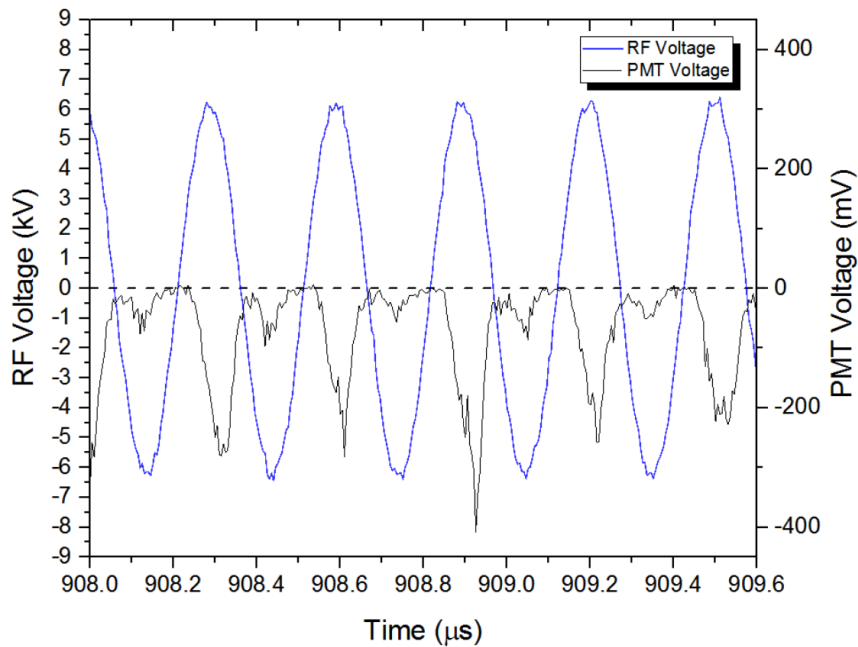
Figure 4.19. PMT and RF signal measured for lanthanated tungsten needle graphed 900 μs after the RF corona onset occurs. Shot 30 for needle L4 [5].

Given the observation of large negative spikes on the PMT signal occuring during the positive needle at times well after corona inception, there was interest in observing whether the needle-plane gap breaks down during the positive polarity like reported for low frequencies [1]. Pushing the RF envelope to a higher maximum voltage, RF breakdown using needle P3 was observed and measured, see Fig. 4.20.
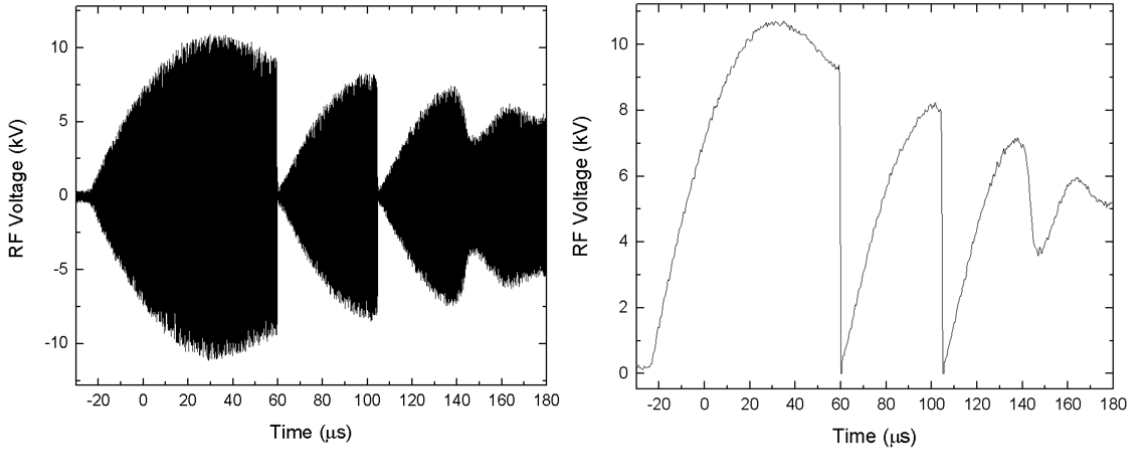
Figure 4.20. RF breakdown raw waveform (left) and envelope (right) over 210 μs time scale. The voltage collapses a total of 3 times. Shot 3 for needle P3 [5].

The voltage of the measured waveform in Fig. 4.20 collapses to zero twice and partially collapses the third time. After the third partial collapse, the voltage stabilizes and remains stable until the RF pulse ends.

The maximum voltage of the applied RF voltage is ~ 10.7 kV. Since the peak exceeds the measured RF corona onset voltages (see Fig. 4.13), it is safe to assume that RF corona ignites during the first rising edge of the applied RF breakdown waveform. When corona ignites in the needle-plane gap, the impedance of the gap partially collapses, resulting in detuning of the RF circuit and reduction of RF voltage. This can clearly be seen in Fig. 4.20 when the RF voltage falls after reaching its peak at the 25 μs mark. At the 60 μs mark, the corona streamers bridge the gap briefly and the voltage collapses to zero, then rises according to the Q of the RF circuit. A more zoomed in look at the point when the voltage initially collapses with a comparison to

zoomed in waveform during a voltage collapse for the 16th shot is shown in Fig. 4.21

.
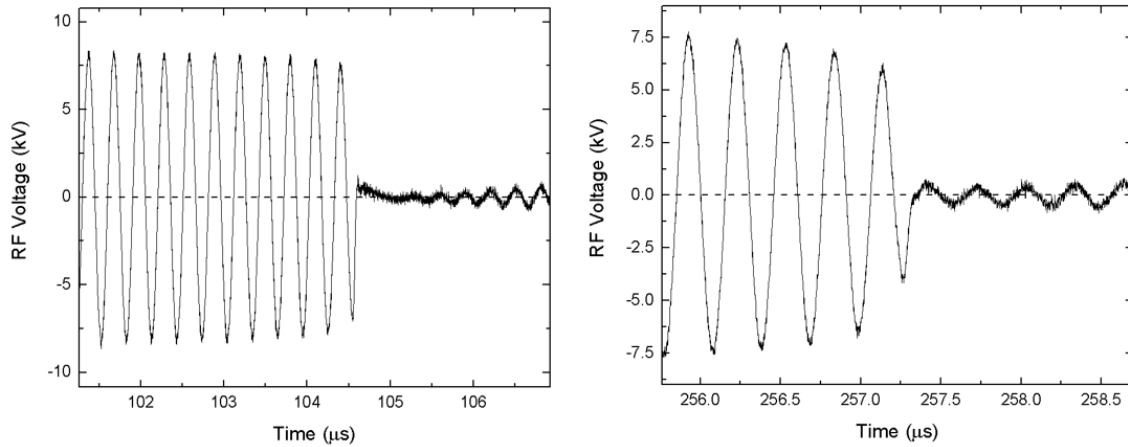
Figure 4.21. Zoomed in RF breakdown waveforms at the point of the first voltage collapse for shots 3 (left) and 16 (right). [5].

The first breakdown for shot 3 occurs when the needle is in the positive polarity. The voltage remains near zero for ~ 500 ns, then begins to rise again. During the last 2 cycles of the RF signal before the voltage collapses, the amplitude decreases slightly. This behavior is evident in all waveforms where a complete or near complete voltage collapse was observed (see right graph of Fig. 4.21). The amplitude of the RF signal decreases earlier and at a faster rate for shot 16. The voltage also does not completely collapse like observed for shot 3. Rather, it retains an amplitude of ~ 500 V before rising again. Nine other measured shots showed similar behavior to shot 16. Only shot 3 yielded a complete voltage collapse. The remaining nine measured shots showed only a partial voltage collapse, where the RF voltage decreases to a lower amplitude briefly, then recovers to an amplitude that falls between the amplitude before the collapse and during the collapse, see Fig. 4.22.
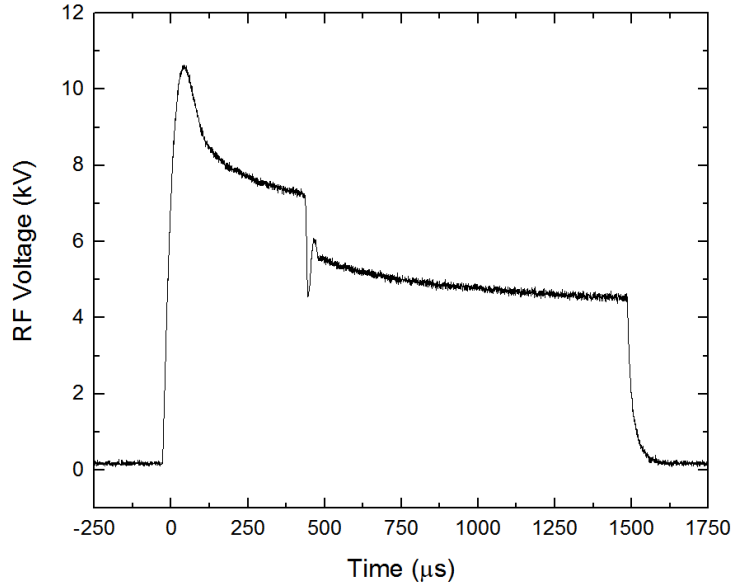
Figure 4.22. RF envelope of shot 1 showing partial collapse of voltage followed by partial recovery of the amplitude.

The behavior of the RF breakdown measured in the needle-plane gap is very different in contrast to the behavior of RF breakdown under a homogeneous field. In a homogeneous field, the RF voltage collapses when breakdown occurs and remains collapsed for the duration of the applied RF voltage, cf. Fig. 3.12. This is due to a sufficient number of charge carriers present in the gap to sustain the arc. The RF corona igniting prior to breakdown also detunes the circuit, which will reduce the maximum voltage the RF circuit can produce. There is still charge accumulation in the needle-plane gap, so the streamers eventually bridge the gap. However, the space charge in the gap is insufficient to support a self sustaining arc. As a result, the discharge returns to corona until sufficient space charge accumulation is achieved.

The half cycle at which the RF breakdown occurs cannot be determined since almost all the measured shots exhibited a rapid decline in amplitude instead of abruptly collapsing. It is noted that RF breakdown in a homogeneous gap does not exhibit preference on the half cycle breakdown occurs on.

CHAPTER 5

CONCLUSION AND FUTURE WORK

5.1   Conclusion

The DC breakdown fields measured for brass and stainless steel electrodes followed reasonably close to measurements reported elsewhere [9,17], providing a good baseline to compare with for RF breakdown. DC breakdown measurements with varying anode and cathode materials confirmed the cathode being a dominant factor in the overall feedback mechanism. It was found that configurations with a brass cathode yielded comparatively lower breakdown field and higher standard deviation than its stainless steel counterpart. Comparing the 3.3 MHz breakdown, the slow-rise RF breakdown fields were approximately 80% of the DC field, matching results from simulation [10] and literature [1]. Fast-rise RF breakdown yielded approximately 90% of the DC breakdown field and is a result of the fast rising field stressing the electrode gap. Pushing the rise time of the RF signal raised the breakdown field to values higher than DC. UV illumination of the gap reduced the standard deviation and amplitude of the RF voltage generated by the faster-rise excitation. Faster-rise RF breakdown measurements with UV application compared reasonably close to breakdown fields calculated by simulation that assumes the inclusion of photon processes. ICCD imaging of the faster-rise breakdown with UV application revealed that RF breakdown tends to favor a single channel. It is postulated that once an ionization event occurs a specific spot, the current will favor that spot and amplify until breakdown occurs.

DC corona measurements using pure tungsten needles with varying included angles revealed that a smaller included angle resulted in a sharp rise in current at lower voltages. Breakdown measured with a positive needle occured at 18 kV, which agrees with what was measured in literature [53]. The negative needle corona did not transition to breakdown, due to the current limit of the high potential tester source used, but it is estimated to occur at 40 kV based on measurements reported

in literature [53].

RF corona measured for pure tungsten needles showed preference on igniting when the needle electrode is negative. In general, there was no distinguishable difference observed in ignition voltage between pure tungsten and lanthanated tungsten needles. A 2D electrostatic simulation of the needle believed to have the most symmetric geometry of all the measured needles, P3, yielded a maximum electric field of 1.65 x 10^8 V/m at the tip, falling short of the necessary magnitude needed for field emission. It is believed that the primary electrons responsible for initiating RF corona in the experiment originate from the volume rather than the needle.

RF breakdown measured in a needle-plane gap did not exhibit a clear indication of which half cycle it starts on like observed for RF breakdown under homogeneous field. Instead, the voltage collapsed and recovered, sometimes more than once during the duration of the applied RF pulse. This is believed to be a consequence of an insufficient amount of charge carriers in the gap to sustain the arc once breakdown occurs.

Using the measured RF breakdown data, the estimated limit for the ESA with a 10 cm gap at 3.3 MHz was calculated at 38 J with a gap voltage of 260 kV (26 kV/cm), which exceeds the 500 kW maximum operating power designated for the ESA [6]. Thus, the ESA can be safely operated at 500 kW with a 20 kV/cm resulting electric field. To avoid corona losses in the ESA while operating at 500 kW, a protrusion with a 0.05 mm radius must not be any higher than 0.07 mm. Thus, the smoothness of the surfaces of the ESA should be carefully considered when selecting materials for construction, especially for the capacative parallel plate gap.

5.2   Future Work

To expand upon this work, RF corona may be studied using a more realistic geometry that can present itself in the ESA. The realistic geometry can take the form of a small protrusion fixed onto the surface of one of the electrodes in a plane-plane electrode geometry. The electrodes could be designed and manufactured in such a way

where one kind of protrusion geometry can be switched out for another. Electrode configurations employing different protrusion geometries could then be compared with analytical or empirical equations given for geometries in literature.

Another possible route would be to do a more thorough study on the role of cathode materials and electrode size in the feedback mechanism for Townsend based DC breakdown. Various metals encompassing a wider range of work functions, for instance, ranging from ytterbium (2.6 eV) to copper (4.7 eV), could be made into electrodes of varying sizes to study the variability and magnitude of the measured DC breakdown. The electrode configurations tested could also be fed with fast DC impulses to see the material/size effects on streamer based breakdown.

BIBLIOGRAPHY

[1] E. Nasser. *Fundamentals of Gaseous Ionization and Plasma Electronics*. Wiley, 1971.

[2] G. G. Raju. *Fundamentals of Gaseous Ionization and Plasma Electronics*. CRC Press, Boca-Raton, 2006.

[3] David M. Pozar. *Microwave Engineering*. Wiley, 2012.

[4] I. A. Aponte, B. Esser, Z. C. Shaw, J. C. Dickens, J. J. Mankowski, and A. A. Neuber. Fundamental study of dc and rf breakdown of atmospheric air. *Physics of Plasmas*, 26:123512, 2019.

[5] I. A. Aponte, B. Esser, J. C. Dickens, J. J. Mankowski, and A. A. Neuber. Fundamental investigation of unipolar and rf corona in atmospheric air. *Unpublished*, 2020.

[6] Benedikt Esser. *Inductively Coupled, Electrically Small Antenna for Ionospheric Heating*. PhD thesis, Texas Tech University, 2020.

[7] J. Stephens. A multi-term boltzmann equation benchmark of electron-argon cross-sections for use in low temperature plasma models. *Journal of Physics D: Applied Physics*, 51(12):125203, 2018.

[8] M. P. Sarma and W. Janischewskyj. D.c. corona on smooth conductors in air. steady-state analysis of the ionisation layer. *Proceedings of the Institution of Electrical Engineers*, 116(1):161–166, 1969.

[9] H. Lau. *Landolt-Börnstein: Zahlenwerte und Funktionen aus Physik, Chemie, Astronomie, Geophysik und Technik*. Springer-Verlag, Berlin, 1957.

[10] H. K. Nguyen, J. J. Mankowski, J. C. Dickens, A. A. Neuber, and R. P. Joshi. Model predictions for atmospheric air breakdown by radio-frequency excitation in large gaps. *Physics of Plasmas*, 24:073505, 2017.

[11] Y. P. Raizer. *Gas Discharge Physics*. Springer-Verlag, 1991.

[12] E. Kuffel, W. S. Zaengl, and J Kuffel. *High Voltage Engineering: Fundamentals*. Butterworth-Heinemann, 2000.

[13] B. Gänger. *Der Elektrische Durchschlag von Gasen*. Springer, 1953.

[14] David Wetz, J. Mankowski, J. Dickens, and M. Kristiansen. *The Impact of Field Enhancements and Charge Injection on the Pulsed Breakdown Strength of Water*. PhD thesis, Texas Tech University, 2006.

[15] Princeton Instruments. Pi-max 4 iccd cameras. https://www.princetoninstruments.com/wp-content/uploads/2020/04/PIMAX4_brochure.pdf.

[16] S. Gossel and C. Leu, editors. *Electrical Breakdown of Short Spark Gaps with Several Electrode Materials in Atmospheric Air at AC (50Hz) and Ramp Voltage (10kV/μs)*, Pilsen, Czech Republic, 2015. 19th International Symposium on High Voltage Engineering.

[17] H. Ritz. Durchschlagfeldstärke des homogenen Feldes in Luft. *Archiv für Elektrotechnik*, 26(4):219–232, 1932.

[18] Spectral Instruments. What is a ccd? http://www.specinst.com/$What_Is_{AC}CD$.html.

[19] B. Esser, D. Mauch, J. Dickens, J. Mankowski, and A. A. Neuber. Tunable, electrically small, inductively coupled antenna for transportable ionospheric heating. *Radio Science*, 53:496–508, 2018.

[20] B. Esser, J. J. Mankowsksi, J. C. Dickens, and A. A. Neuber. Geometry tuning of an electrically small antenna for ionospheric heating. *Radio Science*, 54:494–502, 2019.

[21] D. Rodriguez, G. Gopinathan, R. S. Gorur, and P. Hansen, editors. *Effect of VLF/LF Frequency and Humidity on the Breakdown of Air*, Vancouver, British Columbia, 2007. 2007 Annual Report - Conference on Electrical Insulation and Dielectric Phenomena.

[22] Y. Yang, C. Yuan, and B. Qian. Measurement of s-band microwave gas breakdown by enhancing the electric field in a waveguide. *IEEE Transactions on Plasma Science*, 40(12):3427–3423, 2012.

[23] L. E. Reukema. The relation between frequency and spark-over voltage in a sphere-gap voltmeter. *Transactions of the American Institute of Electrical Engineers*, 27(1):38–48, 1928.

[24] Karl. K. Darrow. Contemporary advances in physics, xxiv high-frequency phenomena in gases, first part. *The Bell System Technical Journal*, 11(4):576–607, 1932.

[25] E. W. Seward. The electrical strength of air at high frequencies. *Journal of the Institution of Electrical Engineers*, 84(506):288–292, 1939.

[26] N. Sata and S.C Haydon. Time-resolved observations of rf corona in air and nitrogen. *Journal of Physics D: Applied Physics*, 17(10):2009–2021, 1984.

[27] Y. Sakiyama and D. B. Graves. Corona-glow transition in the atmospheric pressure rf-excited plasma needle. *Journal of Applied Physics*, 39(16):3644–3652, 2006.

[28] I. E. Kieft, E. P. v d Laan, and E. Stoffels. Electrical and optical characterization of the plasma needle. *New Journal of Physics*, 6:149, 2004.

[29] E. Stoffels, A. J. Flikweert, W. W. Stoffels, and G. M. W. Kroesen. Plasma needle: a non-destructive atmospheric plasma source for fine surface treatment of (bio)materials. *Plasma Sources Science and Technology*, 11(14):383–388, 2002.

[30] F. Auzas, P. Tardiveau, V. Puech, M. Makarov, and A. Agneray. Heating effects of a non-equilibrium rf corona discharge in atmospheric air. *Journal of Physics D: Applied Physics*, 43(49):495204, 2010.

[31] F. Auzas, M. Makarov, and G. V. Naidis. Modelling of pulsed rf corona discharges in high-pressure air. *Journal of Physics D: Applied Physics*, 45(13):135202, 2012.

[32] W. O. Price, J. Drapala, D. V. Thiel, and R. G. Olsen. Corona onset voltage at 60 hz and at high frequency for an isolated cylindrical monopole. *IEEE Transactions on Electromagnetic Compatibility*, 50(3):476–484, 2008.

[33] M. A. Harrison and R. Geballe. Simultaneous measurement of ionization and attachment coefficients*. *The Physical Review*, 91(1):1–7, 1953.

[34] K. Masch. Über Electronenionisierung von Stickstoff und Luft bei geringen und höhen Drucken. *Arch. Elektrotech*, 26:587–596, 1932.

[35] F. H. Sanders. Measurement of the townsend coefficients for ionization by collision. *The Physical Review*, 44:1020–1024, 1933.

[36] H. Hertz. Ueber einen Einfluss des ultravioletten Lichtes auf die electrische Entladung. *Annalen der Physik*, 19:782–816, 1887.

[37] A. Einstein. Über einen Erzeugung und Verwandlung des Lichtes betreffenden heuristischen Gesichtspunkt. *Annalen der Physik*, 17:132–148, 1905.

[38] R. H. Fowler and L. W. Nordheim. The effect of the image force on the emission and reflexion of electrons by metals. *Proc, Roy. London Soc.*, A 121:626–639, 1928.

[39] J. Orloff. *Handbook of Charged Particle Optics*. CRC Press, Boca-Raton, 2008.

[40] Z. C. Shaw, L. Silvestre, T. Sugai, J. J. Mankowski, J. C. Dickens, and A. A. Neuber. On the limits of multipactor in rectangular waveguides. *Physics of Plasmas*, 27(0):038512, 2020.

[41] F. Paschen. Über die zum Funken, Wasserstoff und Kohlensäure bei verschiedenen Drucken erforderliche Potentialdifferenz. *Annalen de Physik*, 273(5):69–75, 1889.

[42] F. M. Bruce. High-voltage spark discharges. *Endeavour*, 13(50):61–71, 1954.

[43] W. Holzer. Über den Stoßdurchschlag der Luft im gleichförmigen Felde bei größeren Elektrodenabständen. *Archiv für Elektrotechnik*, 26(12):865–874, 1932.

[44] L. A. Viehland and E. A. Mason. Transport properties of gaseous ions over a wide energy range. 4. *Atomic Data and Nuclear Data Tables*, 60(1):37–95, 1995. Viehland data base, www.lxcat.net, retrieved on October 28, 2020.

[45] H. W. Ellis, R. Y. Pai, E. W. McDaniel, E. A. Mason, and L. A. Viehland. Transport properties of gaseous ions over a wide energy range. *Atomic Data and Nuclear Data Tables*, 17(3):203, 1976. Viehland data base, www.lxcat.net, retrieved on October 28, 2020.

[46] microwaves101. S-parameters. https://www.microwaves101.com/encyclopedia/s-parameters.

[47] N. G. Trinh. Electrode design for testing in uniform field gaps. *IEEE Transactions on Power Apparatus and Systems*, PAS-99(3):1235–1242, 1980.

[48] R. G. Wilson. Vacuum thermionic work functions of polycrystalline be, ti, cr, fe, ni, cu, pt, and type 304 stainless steel. *Journal of Applied Physics*, 37(6):2261–2267, 2004.

[49] W. Luo, P. Cong, T. Huang, T. Sun, and A. Qiu. Experimental and theoretical studies on the effect of electrode area on static performance of gas switches. *IEEE Transactions On Plasma Science*, 46(7):2558–2561, 2018.

[50] H. G. Krompholz, L. L. Hatfield, A. A. Neuber, K. P. Kohl, J. E. Chaparro, and H.-Y. Ryu. Phenomenology of subnanosecond gas discharges at pressures below one atmosphere. *IEEE Transactions on Plasma Science*, 34(3):927–936, 2006.

[51] G. Edmiston, J. Krile, A. Neuber, J. Dickens, and H. Krompholz. High-power microwave surface flashover of a gas-dielectric interface at 90-760 torr. *IEEE Transactions on Plasma Science*, 34(5):1782–1788, 2006.

[52] L. G. Christophorou and L. A. Pinnaduwage. Basic physics of gaseous dielectrics. *IEEE Transactions on Electrical Insulation*, 25(1):55–74.

[53] A. Roth. *Hoschspannungstechnik*. Springer, 1938.

[54] D. Smith and P. Spanel. Ions in the terrestrial atmosphere and in interstellar clouds. *Mass Spectrometry Reviews*, 14:255–278, 1995.

[55] J. T. Krile and A. A. Neuber. Modeling statistical variations in high power microwave breakdown. *Applied Phyiscs Letters*, 98(21):211502, 2011.

[56] Stanford Computer Optics. Image intensified ccd high speed cameras. https://stanfordcomputeroptics.com/technology/iccd-system-overview.html.

[57] Starizona. How ccd cameras work. https://starizona.com/tutorial/how-ccd-cameras-work/.

APPENDIX A

A   ICCD Camera

An intensified charge-coupled device (ICCD) is a high speed camera capable of photographing events that emits low light. A very simplified diagram of an ICCD camera is shown in Fig. A.1.
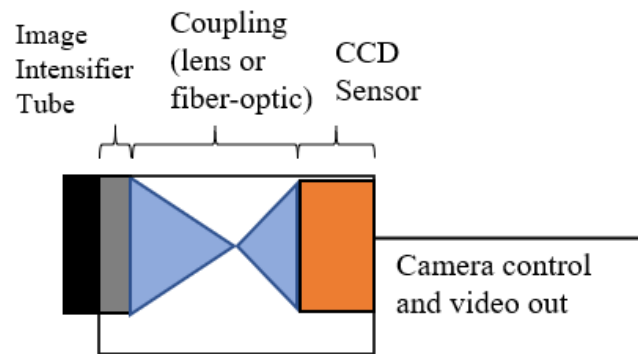
Figure A.1. Simplified diagram of an ICCD camera.

The main components of interest are the image intensifier tube, the coupling between the image intensifier tube and the CCD sensor, and the CCD sensor. The image intensifier tube consists of a photocathode, a microchannel plate (MCP), and a phosphor screen, see Fig. A.2.
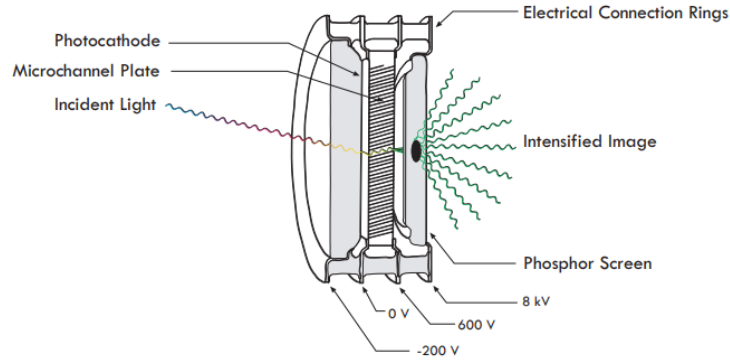
Figure A.2. Layout of an image intensifier tube for ICCD cameras [15].

Incident light first irradiates the photocathode, where a fraction of the photons are converted into photoelectrons via photoemission. The percentage of photoelectrons emitted from the total number of incident photons that irradiated the photocathode is referred to as the quantum efficiency (QE). The QE of the photocathode will vary depending on the wavelength of the incident light.

The emitted photoelectrons then drift towards the MCP. The MCP is a thin structure made of highly resistive material that is covered with small holes called microchannels. The size of the microchannels can be as small as 6 μm and are spaced roughly 15 μm apart from each other. The microchannels are oriented at a small angle (see Fig. A.2) to guarantee that photoelectrons entering them will make a collision with the inner walls. When photoelectrons enter the microchannels, they are accelerated by a constant electric field and impact the inner surfaces multiple times, generating electron avalanches produced by secondary electron emission. It is noted that the biasing of the photocathode with respect to the MCP bias voltage determines whether photelectrons reach the MCP or not. For example, when the photocathode

is biased negatively relative to the MCP, the photoelectrons will be deflected towards the MCP. In the other case where the photocathode is biased more positively than the MCP, the photoelectrons will not reach the MCP. This process of positively and negatively biasing the photocathode with reference to the MCP controls when and how long the image intensifier is turned on and off. This is referred to as gating.

Electron avalanches leaving the MCP then arrive at the phosphor screen. The electrons are absorbed by the phosphor screen and are re-emitted at specific wavelengths. The output of the image intensifier tube is an intensified image of the event you are capturing with the ICCD camera.

The design of an ICCD require the intensified image output to be coupled to the CCD sensor. This can be done by fiber-optically or with a lens, see Fig. A.3.
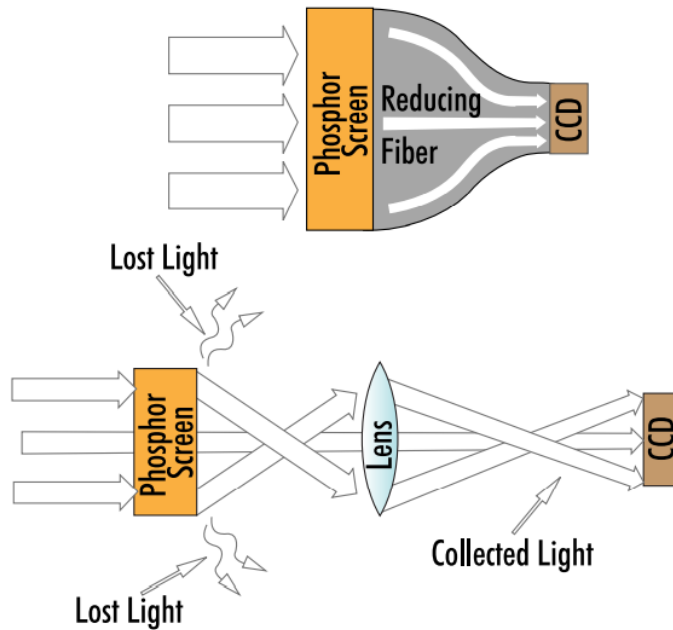
Figure A.3. Fiber-optic coupled (top) and lens-coupled (bottom) configurations [15].

There are distinct advantages and disadvantages between fiber-optic coupling versus lens coupling. For instance, fiber-optic coupled ICCDs yield higher light throughput between the phosphor coating and the CCD sensor (as high as 60%) than lens-coupled ICCDs. [15]. Lens-coupled ICCDS have the option of detaching the image intensifier tube and operate the device as a CCD whereas fiber-optic coupled ICCDs cannot do this since it is more permanent. For more on the performance characteristics of lens-coupling and fiber-optic coupling in ICCD camera, one may refer to [15, 56].

The light of the intensified image finally reaches the CCD sensor. A CCD is an integrated circuit that stores light in the form of an electrical charge and turns it into a digital copy of the light falling onto the CCD [18]. The CCD implements a silicon wafer chip that is separated into thousands of light sensitive squares called photosites [57]. One photosite translates to one pixel in the final digital image produced. A drawing of a single photosite is shown below, see Fig. A.4.
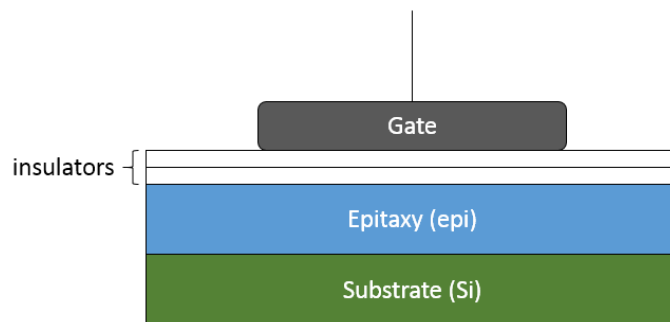
Figure A.4. Diagram of a single photosite in CCD sensor. Insulators: glass layers; Epitaxy: silicon doped with different elements; Substrate: silicon substrate [18].

The charge is generated when the light coming from above the gate strikes the

epitaxial layer, which yields electrons via photoemission. The gate is biased positive with respect to the rest of device to attract electrons towards it. Due to the insulating layer between the epitaxial layer and the gate, the electrons cannot conduct through the gate, resulting in the electrons being held in place. The photosites are bordered by non conducting material which holds the charge generated during the exposure time of the image.

Charge is accumulated for the duration of the exposure time. At the end of the exposure time, the array of photosites will have varying amounts of charge stored in each photosite. A higher amount of charge stored in a photosite translates to a brighter pixel and lower amount of charge stored translates to a darker pixel. The array of photosites may be visualized with the drawing shown in Fig. A.5.
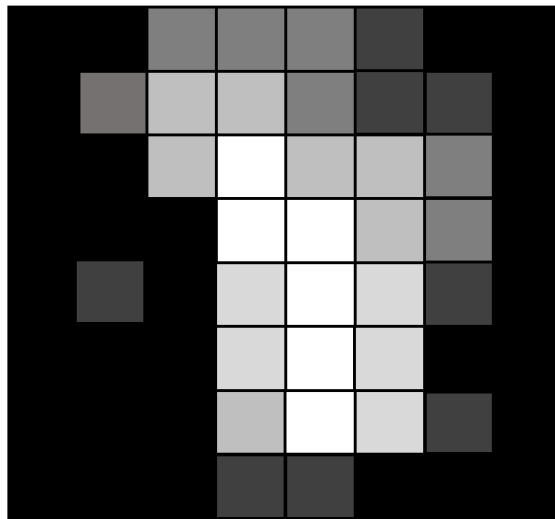
Figure A.5. Drawing of an array of photosites holding charge after the exposure time. Darker square have received less light and hold less charge while brighter squares have received more light and hold more charge.

The stored charges are then moved out of the CCD via parallel and serial shift-

ing [18]. A parallel shift is when the column moves from right to left. A serial shift moves the left most column down from top to bottom and directs the electron packets towards the camera's electronics unit where they are digitized [18, 57]. The digitized electron packets are then displayed on the computer screen in the form of a raw image. Additional processing and filtering may be needed to remove unwanted artifacts resulting from the CCD.